https://doi.org/10.5194/egusphere-2026-3611
Preprint. Discussion started: 26 June 2026

Sensitivity of time-lapse magnetic resonance sounding to vadose zone hydrodynamic parameters: monitoring of an intense meteorological event

Guillaume Gru[1], Jean-François Girard[1], Philippe Ackerer[1], and Nolwenn Lesparre[1]

[1]Institut Terre et Environnement de Strasbourg, University of Strasbourg/EOST/ENGEES, CNRS, UMR7063, Strasbourg, France

Correspondence: Guillaume Gru (gru@unistra.fr)

Abstract. Magnetic Resonance Sounding (MRS) is a geophysical method that provides direct information on subsurface water content and can complement traditional hydrological observations for model calibration. We develop a coupled hydrogeophysical framework by linking one-dimensional unsaturated flow with an MRS forward model to simulate a time-lapse MRS experiment during an infiltration event in the Strengbach headwater catchment in northeastern France. The geometry of the model is conditioned using insights on the porous medium thickness provided by seismic refraction tomography, in order to reduce model uncertainties related to the thickness of subsurface layers. We apply a Global Sensitivity Analysis (GSA) to quantify how uncertainty in hydrodynamic parameters affects MRS signals and their temporal evolution. The GSA combines variance-based Sobol indices with two other moment-based metrics (AMAE and AMAV) to characterize the sensitivity of both the mean and the variance of the MRS signal distributions. Using these complementary metrics provides a more robust assessment of parameter influence than Sobol indices alone. Our results identify the parameters which exert the strongest control on time-lapse MRS signals and reveal how their influence changes during the infiltration event. We also identify parameters whose uncertainties have insignificant contribution to MRS signals. These insensitive parameters are not expected to be precisely estimated with inverse modeling techniques based on MRS data. These insights clarify the potential and limitations of MRS data for constraining hydrological parameters in shallow mountain aquifers and demonstrate how the temporal evolution of MRS sensitivity can be exploited to optimize monitoring strategies during transient hydrological events.

1 Introduction

Water resources in mountainous regions are of primary importance because they supply freshwater to both local and downstream population (Viviroli et al., 2011, 2020). These regions also provide key ecosystem services that depend on water availability, including food and timber production and carbon sequestration (Grêt-Regamey and Weibel, 2020). Mountain environments are especially vulnerable to climatic and socio-economic changes (Immerzeel et al., 2019). Hydrological modeling is a fundamental tool for predicting the effects of climate change on the water resource in these sensitive systems and for supporting sustainable resource management (Haro-Monteagudo et al., 2020; Moraga et al., 2021).

https://doi.org/10.5194/egusphere-2026-3611
Preprint. Discussion started: 26 June 2026

Accurate model parameterization is essential to reduce uncertainty in hydrological predictions. Calibrating hydrological models based on stream discharge solely introduces equifinality issues: several model parametrization resulting in a good fit of the observed data (Ebel and Loague, 2006). Additional constraints can be brought by point-scale observations such as piezometric data. However, in mountainous regions, access difficulties and steep slopes make borehole drilling challenging or impossible. Furthermore, headwater catchments exhibit strong heterogeneities in subsurface hydraulic properties and layer geometry (Benton et al., 2022; Lesparre et al., 2020), which limit the spatial representativity of point-scale measurements. Near surface geophysical methods are valuable in this context because they provide relatively low-cost, non-destructive and distributed additional information on subsurface properties and flow processes (Binley et al., 2015). A wide range of techniques are used to characterize subsurface heterogeneity, including Electrical Resistivity Tomography (ERT, Pleasants et al. (2022)), Seismic Refraction Tomography (SRT, Pasquet et al. (2022)), Ground Penetrating Radar (GPR, Zhang et al. (2022)), microgravimetry (Chaffaut et al., 2022), Magnetic Resonance Sounding (MRS, Legchenko et al. (2020)).

This study focuses on MRS. One of the major advantages of this geophysical method is its direct sensitivity to the water content distribution in the subsurface (Legchenko and Valla, 2002). Most geophysical methods (e.g. ERT and GPR) rely on petrophysical laws to infer the hydrologic properties from measured geophysical variables. MRS data are not burdened by the modeling errors related to these petrophysical models, and they can be directly interpreted in terms of hydrological behavior of the studied object. The vertical measurement footprint of MRS data reaches depths several tens of meters, compared to a few meters for GPR (Legchenko et al., 2018). Time-lapse MRS has been successfully applied to study the dynamics of the subsurface water content (Legchenko et al., 2020, 2022; Mazzilli et al., 2020). Geophysical data can be used in a coupled hydrogeophysical approach to infer the subsurface hydrodynamic parameters (Costabel and Günther, 2014; Lesparre et al., 2020; Moua et al., 2023). While Costabel and Günther (2014) inferred hydrologic parameters from static MRS observations of the capillary fringe in homogeneous sands, recent studies have expanded MRS applications to dynamic or layered systems. For instance, Legchenko et al. (2020) utilized time-lapse MRS measurements for parameter estimation, and Lesparre et al. (2020) characterized aquifer layer thickness and porosity from spatially distributed MRS data. Because a comprehensive analysis and discussion of how MRS signals respond to hydrodynamic parameters is still lacking in these approaches, this study provides a Global Sensitivity Analysis (GSA) of time-lapse MRS signals to bridge this gap and advance hydrogeophysical modeling.

One of the crucial steps in the calibration process of a numerical model is sensitivity analysis. GSA quantifies the effects of the uncertainties in the model parameters, considered as random variables, on the outputs of the model (Saltelli et al., 2007). For the purpose of conciseness and readability, we will describe the effects of the uncertainties in the parameters as the effects of the parameters in the following. GSA is a crucial step in the calibration process because it allows a deep understanding of the studied model (Ferretti et al., 2016; Razavi et al., 2021) and the identification of parameters with little to no influence on the outputs of interest. Those parameters are not expected to be identifiable by observations of the outputs (Wu et al., 2019). Thus, the non-sensitive parameters can be set to experimentally measured or literature-based reference values in order to reduce the parameter space dimension for the parameter estimation procedure (Dell'Oca et al., 2025). GSA is also well suited for dynamic systems, such as those analyzed through time-lapse experiments, where the influence of parameters may vary over time (Maina and Guadagnini, 2018; Younes et al., 2018). It has been widely applied to hydrological models (Song et al., 2015). It was

https://doi.org/10.5194/egusphere-2026-3611
Preprint. Discussion started: 26 June 2026

notably applied to hydrogeophysical models, coupling subsurface flow models and near surface geophysical methods such as GPR (Moua et al., 2023) or gravimetry (Maina and Guadagnini, 2018). Recent studies outlined the limitations of using solely variance-based GSA such as the classical analysis of Sobol indices (Dell'Oca et al., 2017). It is therefore interesting to base the GSA on complementary features of the model outputs probability density function (pdf) such as the mean or higher order statistical moments (Dell'Oca et al., 2025; Maina and Guadagnini, 2018).

We developed a hydrogeophysical model based on Richards 1D water flow equation (Richards, 1931) and the fundamental equations of MRS (Legchenko and Valla, 2002). We define a numerical time-lapse MRS experiment based on real meteorological and hydrological data collected during a meteorological event in the Strengbach headwater catchment (Pierret et al., 2018). This numerical experiment allows us to simulate several acquisition parametrization at a single moment and high acquisition frequencies which are unreachable in realistic field conditions. We address two main questions: (1) Which parameters exert the greatest influence and how does this influence evolve during a significant meteorological event ? (2) Which hydrodynamic parameters have a negligible influence on the MRS signals ? The information gathered by answering these questions is useful for a better use of MRS signals in hydrogeophysical inverse problems and for future experimental design. Taking into account the limitations of variance-based only GSA exposed by the authors of Dell'Oca et al. (2017), we conduct the GSA of our model through Sobol indices (Sobol, 2001), and also through the AMAE and AMAV indices (Dell'Oca et al., 2017): sensitivity indices based on the mean and the variance of the outputs of the model, respectively. Section 2 describes the studied site. Section 3 presents the methodological background, including the subsurface flow model and the MRS method. Section 4 details the GSA methodology. Results are presented in Sect. 5 and discussed in Sect. 6. Finally, Sect. 7 summarizes the main conclusions of this study.

2 Studied site

The numerical experiment we present in this study was designed using data collected on the Strengbach headwater catchment in order to base the test case on realistic mountainous watershed conditions. The Strengbach catchment is located in the Vosges mountains in northeastern France (Fig. 1). It is the experimental site of the Observatoire Hydro-Géochimique de l'Environnement (OHGE, https://ohge.unistra.fr/) which is part of the French critical zone observatories network (OZCAR, https://www.ozcar-ri.org). The OHGE has been collecting hydrological, geochemical and meteorological data on the catchment since 1986 to explore several environmental questions such as the impact of acid rains on forests or the water resources in a mid-mountainous context (Pierret et al., 2018). Such long term observations allowed the assessment of the effects of local climate change on the hydrological cycle of the catchment (Strohmenger et al., 2022) and the projection of future effects of climate change on both the water cycle and the vegetation cover (Beaulieu et al., 2016).

The Strengbach is a small forested catchment covering an area of 0.8 km^2, with an altitude ranging between 880 and 1150 m a.s.l. The bedrock is mainly composed of fractured granite. The lithology of the catchment also shows outcrops of microgranite and gneiss bodies along the southern and northern slopes (Pierret et al., 2018). We describe the subsurface compartments as follows: above the bedrock is a granitic saprolite above which lies a soil layer. Soils are very coarsely grained,

https://doi.org/10.5194/egusphere-2026-3611
Preprint. Discussion started: 26 June 2026

sandy and rich in gravel (Fichter et al., 1998). The layers' thicknesses show strong heterogeneities at the catchment scale. A recent study used SRT to infer the depths of the boundaries between soil, saprolite, and bedrock layers from compression P-wave velocities (Lesparre et al., 2024). Saprolite thickness varies from 4 ± 1 m to 12 ± 1.4 m and soil thickness from 1.4 ± 0.5 m to 3.4 ± 1.1 m. Local climatic conditions are temperate oceanic mountainous, with a mean precipitation of 1380 mm.yr^{-1}, and a mean annual temperature of 6°C in the period 1986 to 2015. During that same period, mean potential evapotranspiration was of 571 mm.yr^{-1}, with values ranging between 516 and 729 mm.yr^{-1}, and the mean discharge at the stream outlet was about 750 mm.yr^{-1}, with variations ranging from 494 to 1132 mm.yr^{-1} (Pierret et al., 2018).

We focus on a relatively flat zone above the main spring of the Strengbach catchment (Fig. 1), where the subsurface below the soil consists of colluvium (Pierret et al., 2018). This area features the catchment's thickest saprolite ($\approx$ 13 m, Lesparre et al. (2024)), forming a thick weathered zone that hosts a shallow unconfined aquifer well-suited for 1D hydrological modeling. Indeed, the moderate slope, the relatively high soil permeability, the water-table depth, and the observed dynamics are all consistent with the vertical infiltration assumed in such 1-D models. Previous research underscores the hydrological significance of this zone. For instance, MRS mapping identified it as having the highest subsurface water content in the entire catchment (Boucher et al., 2015), while time-lapse micro-gravimetry revealed intense localized water dynamics (Chaffaut et al., 2022). Furthermore, numerical experiments by Lesparre et al. (2020) showed that this zone is particularly well-suited for time-lapse MRS monitoring due to the high expected magnitude of signal variations.

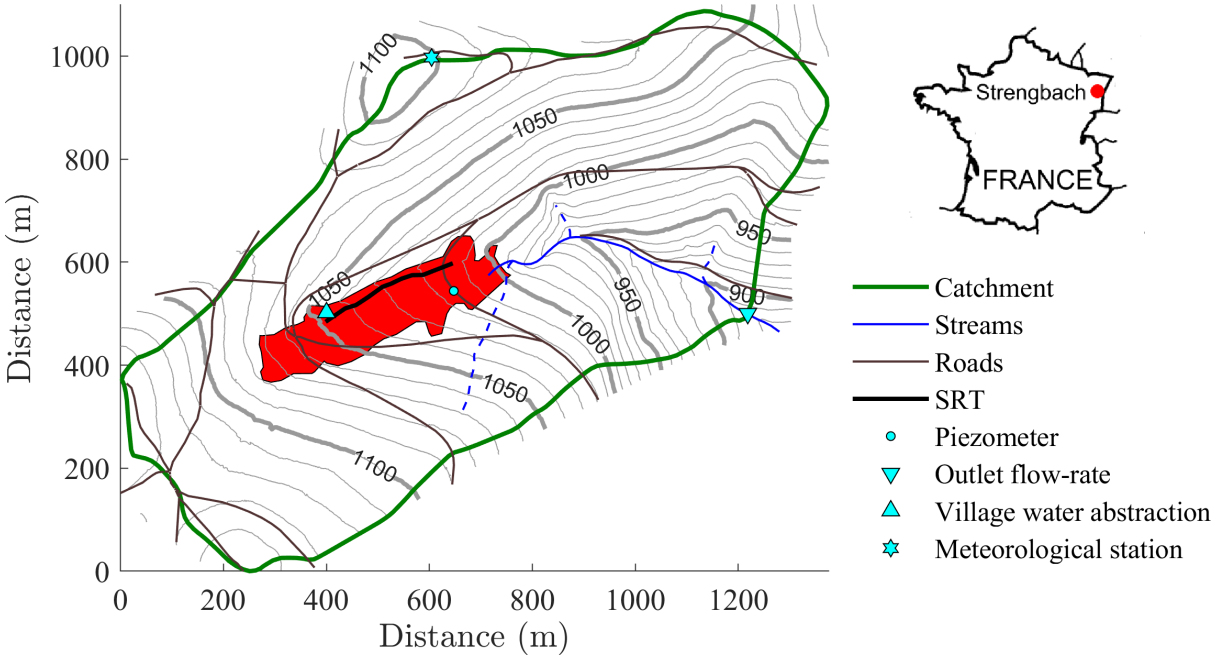

Figure 1. Map of the Strengbach headwater catchment, northeastern France. The studied area is highlighted in red.

https://doi.org/10.5194/egusphere-2026-3611
Preprint. Discussion started: 26 June 2026

3 Background

3.1 1D subsurface flow model

We model the one-dimensional subsurface flow using the so-called "mixed" form of Richards' equation (Gilding, 1991):

$$\frac{\partial \theta}{\partial t} - \frac{\partial}{\partial z}\left[K(h)\left(\frac{\partial h}{\partial z} - 1\right)\right] = f, \tag{1}$$

where θ ($\mathrm{m}^3.\mathrm{m}^{-3}$) is the water content, t (s) is the time, z (m) is the depth, positive downwards, K ($\mathrm{m.s}^{-1}$) is the hydraulic conductivity of the medium, h (m) is the pressure head, and f ($\mathrm{m}^3.\mathrm{m}^{-3}.\mathrm{s}^{-1}$) is a source/sink term. Along with Richards' equation, the hydrologic model uses Van Genuchten's (VG) model to define the pressure-water content relationship (Van Genuchten, 1980) and Mualem's model for the pressure-hydraulic conductivity relationship (Mualem, 1976). Those models write:

$$\theta(h) = \begin{cases} \theta_r + (\theta_s - \theta_r)\left(1 + |\alpha h|^n\right)^{-m} & \text{if } h < 0, \\ \theta_s & \text{if } h \geq 0, \end{cases} \tag{2}$$

$$K(S_e(h)) = \begin{cases} K_s S_e(h)^L \left[1 - \left(1 - S_e(h)^{\frac{1}{m}}\right)^m\right]^2 & \text{if } h < 0, \\ K_s & \text{if } h \geq 0, \end{cases} \tag{3}$$

where θ_r ($\mathrm{m}^3.\mathrm{m}^{-3}$) is the residual water content, θ_s ($\mathrm{m}^3.\mathrm{m}^{-3}$) is the saturated water content, α (m^{-1}) is a parameter related to the mean pore size, n (-) is the pore distribution index, m is a parameter defined as $m = 1 - 1/n$, K_s ($\mathrm{m.s}^{-1}$) is the saturated hydraulic conductivity, S_e (-) is the effective saturation:

$$S_e(h) = \frac{\theta(h) - \theta_r}{\theta_s - \theta_r}, \tag{4}$$

and L (-) is a parameter related to the tortuosity, set here to 0.5.

In order to solve the temporal evolution of the water content with this model, one needs to define the initial state of the system (the pressure head distribution $h(z, t = 0\ \mathrm{s})$) and boundary conditions. We use two types of boundary conditions: Dirichlet (imposed pressure head) at the bottom of the subsurface column and Neumann (imposed flux) at the surface. The numerical solution of Richard's equation is computed with Phydrus (Collenteur et al., 2020), a python library based on HYDRUS-1D finite element flow equation solver (Šimůnek et al., 2008).

The hydrologic model boundary conditions (BCs) are constrained by meteorological and hydrological data measured on the Strengbach catchment. The lower BC is a time-variable pressure condition. The water table depth z_{table} (m) is measured hourly in a piezometer within the studied area (Fig. 2d). The water table depth value is always under 7 m. Therefore, we set the maximum depth of the zone where unsaturated water flow equations are solved to $z_{max} = 7$ m. Piezometric measurements give local information and we are studying a relatively large area (Fig. 1). Therefore, we introduce the parameter Δh_{piezo} (m)

https://doi.org/10.5194/egusphere-2026-3611
Preprint. Discussion started: 26 June 2026

in the GSA to take into account uncertainties on z_{table}. This parameter is considered as a random variable and we analyze its effects on MRS output signals along with hydrodynamic parameters. The pressure at the bottom of the soil column is $h(z = z_{max}, t) = z_{max} - z_{table}(t) + \Delta h_{piezo}$. The upper BC is modeled from precipitations and meteorological data measured at the summit weather station of the catchment. The time variable upper flux BC $Q_{top}(t)$ (mm.s^{-1}, cumulated to a daily time-step in Fig. 2c) is obtained by taking into account several surface processes:

$$Q_{top}(t) = R(t) + Q_s(t) - E(t) - Tr(t) - R_s(t), \tag{5}$$

where R is the flux due to rain infiltration, Q_s is the snowmelt infiltration flux, E is the soil evaporative flux, Tr is the transpiration flux, and R_s is the surface runoff, all fluxes in mm.s^{-1}. The Strengbach catchment exhibits a strong drainage capacity and surface runoff is negligible. Thus, within the scope of this study, we set $R_s(t) = 0$ mm.s^{-1}, for all t.

The first two terms (i.e. R and Q_s) depend on effective precipitation: the portion of precipitations that reaches the ground. They require to model precipitations interception by the vegetation cover and to substract it from measured precipitations. The evapotranspiration components (i.e., E and Tr), which correspond to Actual Evapotranspiration (AET) in Eq. (5), are in fact estimated based on the Potential Evapotranspiration (PET), the available water content and the vegetation state. The computation of PET is based on the Penman model. For details on the PET computation procedure, see Belfort et al. (2025) and references therein. Whereas PET is computed only from meteorological variables, AET takes into account the availability of water in the root system zone and vegetation parameters. AET and interception are computed using a reservoir based model which takes into account several ecophysiological processes in order to compute AET from PET (for details on the computation of interception and AET, see Granier et al. (1999) and references therein). Interception and AET are computed with a daily time step (Fig. 2a) and interpolated to the hourly time step (based on the timing of the precipitations and the length of the day respectively) for hydrological simulation. Interception is deducted from raw precipitation in order to get effective precipitation (Fig. 2b). A temperature-based snowpack model is used to implement the precipitation infiltration delay due to the accumulation of a snow layer on the ground surface. The snowpack model was adapted from the Hydrologiska Byråns Vattenbalansavdelning (HBV - Hydrological Bureau Water Balance Department) hydrological model (Lindström et al., 1997). The effective precipitation phase (snow, rain or mixed phases) depends on the measured temperature. We define two threshold temperatures for this purpose: T_{min} (°C) the temperature below which all precipitations are in solid phase, and T_{max} (°C) the temperature above which all precipitations are in liquid phase. For temperatures between T_{min} and T_{max}, the fraction of solid precipitations varies linearly between 1 and 0. We consider $T_{min} = -3$ °C and $T_{max} = 1$ °C. The liquid precipitations directly infiltrate the soil and the solid precipitations accumulate in a snowpack and melt generating the snowmelt infiltration flux Q_s. The mean temperature of the snowpack T_s (°C) is computed as follows:

$$T_s(t) = k_1 T_s(t - \Delta t) + (1 - k_1) T(t), \tag{6}$$

where k_1 (-) is a user defined weighting factor, Δt (s) is the time step and T (°C) is the air temperature. We set $k_1 = 0.3$ (Lindström et al., 1997) and the time step Δt corresponds to the weather variables measurement time step: 3600 s. The

https://doi.org/10.5194/egusphere-2026-3611
Preprint. Discussion started: 26 June 2026

accumulated snowpack melts under two conditions: (1) the air temperature is higher than 0°C, and (2) $T_s = 0$ °C. If these two conditions are met, the snowmelt flux is computed as follows:

$$Q_s(t) = k_2\, T(t), \tag{7}$$

where k_2 (mm.s^{-1}.°C^{-1}) is the degree-day factor parameter, set to 0.1 mm.s^{-1}.°C^{-1} in this study (Lindström et al., 1997).

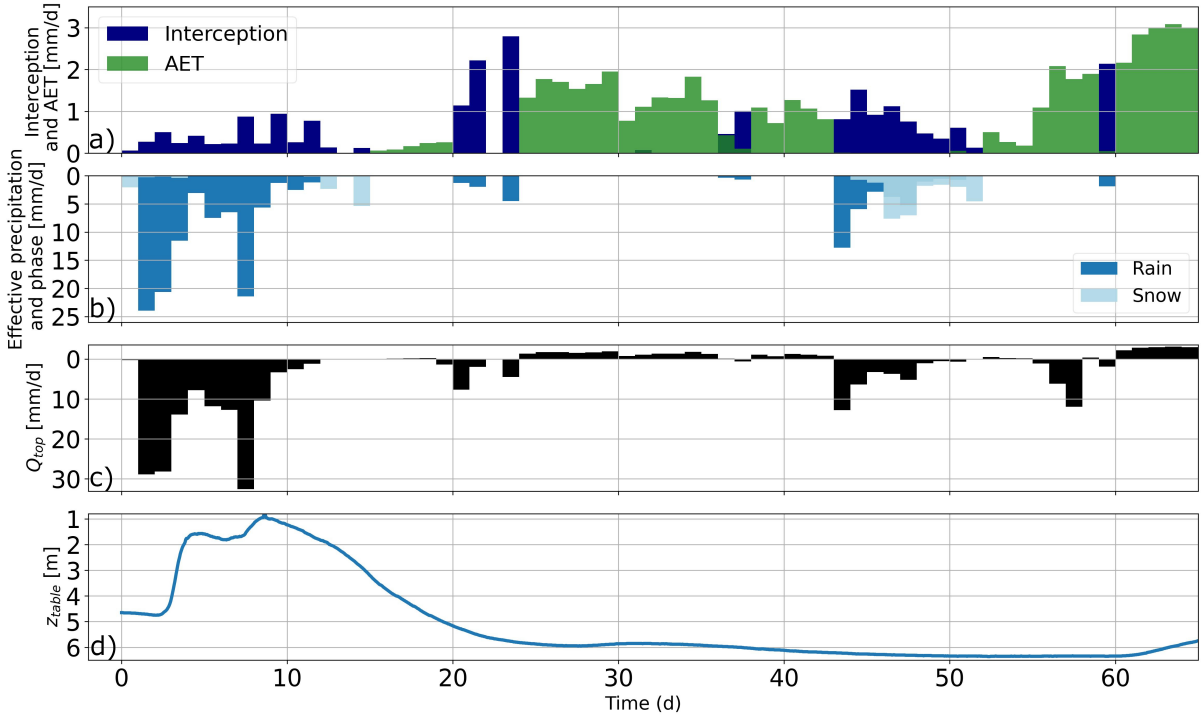

Figure 2. Time series of the hydrological and meteorological data constraining the model boundary conditions: a) interception and AET, b) effective precipitation, c) surface flux Q_{top}, and d) water table depth z_{table} measured in a piezometer within the studied area.

We set our study in winter 2021, since an intense meteorological event occurred this year. We observed an intense rise in the water table level measured in the piezometer at the end of January and early February (Fig. 2d). Such a fast and important saturation of the medium can be particularly interesting to understand the saturation/unsaturation behavior of the shallow aquifer we study. This extreme hydrological event is due to two main drivers. Firstly, a strong and long-lasting rain event: effective precipitations were higher than 20 mm.d^{-1} at most and reached 107 mm cumulated over a period of 12 days. Secondly, it is due to the accumulation of a snow cover before the rain event: the measured snowpack height reached 0.8 m. A rise in the temperature and the rain event triggered the melt of this snow cover. We notice this coupled effect by comparing Fig. 2b and Fig. 2c: during the period from day one to day 12 (day zero is set to the 26^{th} of January 2021), the modeled infiltration flux is larger than the effective precipitation. Prior to the accumulation of this snow cover, the weather was dry. In this context, we simulated MRS measurements every 24 hours during a time period of 66 days in order to analyze both the short term

https://doi.org/10.5194/egusphere-2026-3611
Preprint. Discussion started: 26 June 2026

and mid-term effects of the meteorological event on the sensitivity of MRS signals to hydrodynamic parameters. We consider a model warm-up period starting on the first of November 2020 in order not to define arbitrarily the initial condition of the simulation.

We set the boundaries between underground compartments (soil, saprolite, bedrock) using prior information obtained by SRT. The whole catchment was investigated in 2018 and 2019 with SRT (Lesparre et al., 2024). One of the SRT profiles is located within the area we examine in this study (Fig. 1). We use the boundaries' depths inferred in Lesparre et al. (2024) for this SRT profile: $z_{Soil/Sapro} = 2.1$ m , $z_{Sapro/Bedrock} = 15$ m (Fig. 3). Subsurface material is expected to be highly altered close to the surface and less and less altered towards the bedrock. Still, there might be a non-negligible water content in the saturated zone below z_{max}. Thus, we introduce a permanently saturated zone where the water content is constant: $\forall z > z_{max}\ \theta(z) = \theta_s(z)$. This zone ranges from depth $z_{max} = 7$ m to $z_{max,MRS} = 50$ m. We set the maximum depth of the subsurface column to 50 m as the granitic bedrock is altered and fractured down to depths of several tens of meters (Lajaunie et al., 2023) and to consider fully the region investigated by MRS measurements.

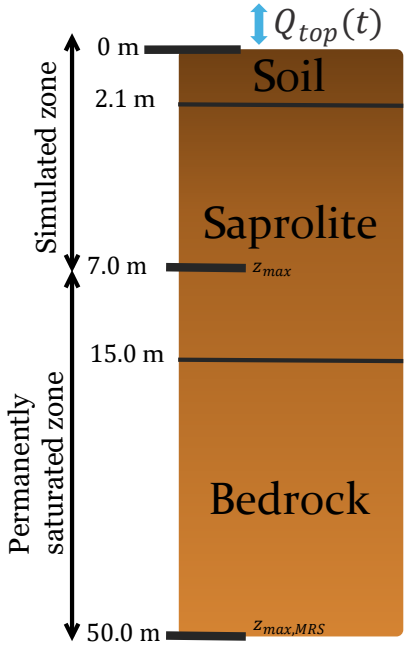

Figure 3. Schematic representation of the subsurface model. The underground porous medium is divided in three layers, from surface to depth: the soil, the saprolite and the bedrock. The hydrogeophysical model considers two compartments: a simulated zone where the unsaturated water flow equations are solved numerically and a permanently saturated zone where $\theta(z) = \theta_s(z)$.

3.2 MRS method and modeling

MRS uses the magnetic properties of the protons in hydrogen atoms composing the subsurface water molecules. Under natural conditions, the macroscopic magnetization vectors of the protons align with Earth's magnetic field (Legchenko and Valla,

https://doi.org/10.5194/egusphere-2026-3611
Preprint. Discussion started: 26 June 2026

2002). The generation of an alternating electrical current in a wire loop placed on the ground induces a perturbing electromagnetic field that tilts the protons' magnetization vectors away from their equilibrium state. The product of the injected current intensity and the emission duration is defined as the electromagnetic pulse q (A.ms). Both the pulse and the geometry of the loop control the investigated depth of the MRS sounding: larger loops and stronger electromagnetic pulses result in deeper investigation. The frequency of the electromagnetic field is set to Larmor frequency, which is the precessional frequency of hydrogen protons. The perturbing electromagnetic field is then shut down, and the protons relax back to their equilibrium state. The oscillations of the magnetization vectors around Earth's magnetic field at Larmor frequency during relaxation generates an electromagnetic field. This field induces in turn an electrical current in the wire loop. The voltage measured in the loop is proportional to the subsurface water content (Legchenko and Valla, 2002).

The envelope of the signal measured in the loop is multi-exponentially decaying (Hertrich et al., 2005):

$$E(t,q) = \int_z \int_{T_2^*} \kappa(q,z)\theta_{MRS}(z,T_2^*)e^{-\frac{t}{T_2^*(z)}} dT_2^* dz, \tag{8}$$

where $\kappa(q,z)$ (nV.m^{-1}) is the sensitivity function, θ_{MRS} (-) is the water content which can be detected by MRS, T_2^* (s) is the exponential relaxation characteristic time. Assuming a mono-exponential behavior and evaluating Eq. (8) at time $t = 0$ s leads to the following equation:

$$E_0(q) = \int_z \kappa(q,z)\theta_{MRS}(z)dz. \tag{9}$$

This study focuses on the sensitivity of $E_0(q)$ to hydrodynamic parameters. The sensitivity function κ depends on several parameters: the geometry of the loop, the electrical resistivity of the subsurface, and the local geomagnetic field. We consider an eight-shaped loop made of two squares meeting at a common corner, each with a side length of 40 m. This loop layout was used on previous MRS investigations of the catchment (Boucher et al., 2015). The considered loop is located on a single pedological unit (the colluvium zone, highlighted in red in Fig. 1). Therefore, we assume that the scale of lateral heterogeneities in subsurface properties is larger than the MRS measurement footprint. Thus, the coupled 1D hydrogeophysical model is consistent with the studied field properties. For the purpose of this study, a reference sensitivity function κ_{ref} (Fig. 4) is computed with the software Samovar (Legchenko and Shushakov, 1998) using the above-mentioned parameters, as well as a maximum depth (i.e. $z_{max,MRS}$), and boundaries for the pulse interval. Then, the reference sensitivity function κ_{ref} is interpolated to correspond to the spatial discretization of the hydrologic model and the experimental pulse values. The water content profiles $\theta(z)$ computed with the hydrological model described in Sect. 3.1 are used to compute MRS signals with a numerical integration of the integral in Eq. (9). The numerical experiment introduced in this work aims to analyze the sensitivity of the system's response to variations in hydrodynamic parameters across five distinct pulse values. This representative subset was selected to ensure a thorough GSA while maintaining computational efficiency. The electromagnetic pulse values are spaced evenly on a logarithmic scale on the interval $[60, 2260]$ A.ms: $(q1, q2, q3, q4, q5) = (60, 145, 362, 904, 2260)$ A.ms. This

https://doi.org/10.5194/egusphere-2026-3611
Preprint. Discussion started: 26 June 2026

logarithmic pulse moment spacing is typical for MRS acquisition sequences. The pulse values control the depth of investigation through the MRS sensitivity function κ (Fig. 4). The depths of maximum sensitivity $z_{s,max}(q_i)$ ($i \in \{1, ..., 5\}$) are $z_{s,max}(q_1) =$ 0.7 m, $z_{s,max}(q_2) = 1.6$ m, $z_{s,max}(q_3) = 4.1$ m, $z_{s,max}(q_4) = 10.0$ m, $z_{s,max}(q_5) = 20.0$ m. These depths are represented with crosses in Fig. 4.

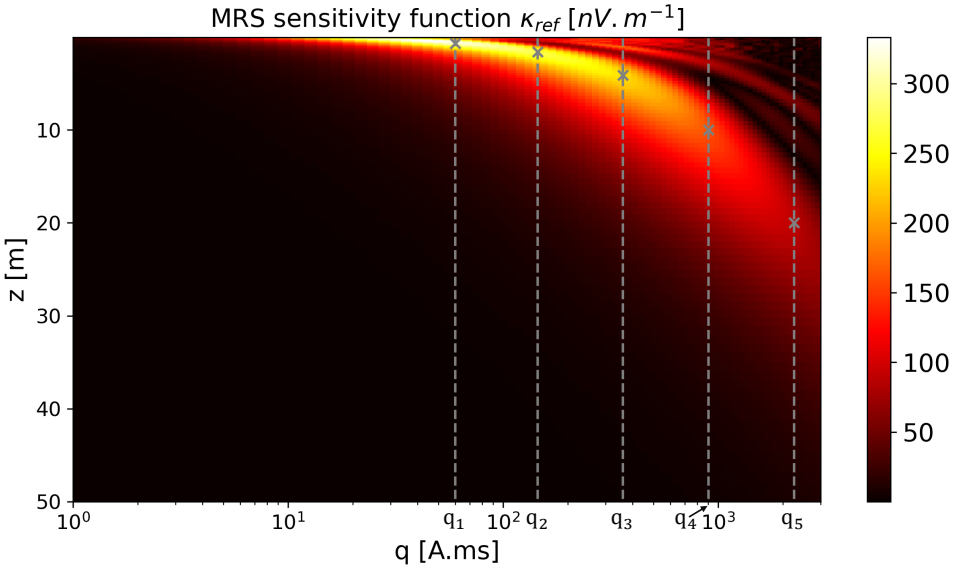

Figure 4. Reference MRS sensitivity function $\kappa_{ref}(q, z)$ computed with Samovar (Legchenko and Shushakov, 1998). Vertical dashed lines represent the simulated pulse moments, crosses are placed at the depths of maximal sensitivity for each pulse.

The subscript MRS is added to the water content variable in Eq. (8) and Eq. (9) because the MRS method is not sensitive to the entire water content in the subsurface (Lubczynski and Roy, 2003; Boucher et al., 2011). The MRS measurement devices have an instrumental dead time: the time needed to switch the device from emitting to receiving mode. This instrumental dead time is fixed at 3.10^{-2} s for the device considered in this study: NUMISplus (IRIS instruments). The water with a relaxation time T_2^* shorter than - or very close to - the instrumental dead time cannot be detected by this MRS equipment. Several physical and hydrological properties have an influence on the relaxation time. Boucher et al. (2011) carried out a laboratory experiment in order to quantify the effects of (1) grain size distribution, (2) clay content, and (3) saturation degree on the fraction of MRS undetectable water content (denoted as $\theta_{u\%}$, i.e. $\theta_{MRS} = \theta \times (1 - \theta_{u\%})$). They showed that $\theta_{u\%}$ is firstly sensitive to saturation: in the driest samples, $\theta_{u\%} \approx 50 - 60\%$, depending on grain size distributions. When the saturation increases, $\theta_{u\%}$ decreases. Then a saturation threshold around 40% is reached, and the value of $\theta_{u\%}$ is minimal ($\approx 10 - 20\%$). For saturations above this threshold, $\theta_{u\%}$ remains almost constant. This behavior is reproduced in Fig. 5. The strong control of saturation over the relaxation time, and thus on MRS undetectable water content, is due to increased interactions between water molecules and the solid grains under low saturation. The effects of grain size distributions and clay contents were measured on saturated samples. $\theta_{u\%}$ is the smallest for the largest grain size; it increases as the median grain size decreases. It reaches a maximum of 16%

https://doi.org/10.5194/egusphere-2026-3611
Preprint. Discussion started: 26 June 2026

for a median grain size around 0.1 mm and decreases for smaller grains. Concerning the effects of clay content, we consider the results for the samples with a clay content below 20% as it corresponds to measured soil granulometry in the Strengbach catchment (Belfort et al., 2018; Oursin et al., 2023; Belfort et al., 2025). In these samples, the higher the clay content is, the higher $\theta_{u\%}$ is. This increase is stronger for coarser grains. Considering the combined effects of grain size distribution, clay content, and saturation degree in our hydrogeophysical model, we implement MRS water content as follows:

$$\theta_{MRS}(z) = \theta(z) \times (1 - \theta_{u\%}(S_e(z), \theta_{u\%,base}, \theta_{u\%,max}, S_{lim})), \tag{10}$$

with $\theta_{u\%} \in [0, 1]$. We implement $\theta_{u\%}$ as a function of effective saturation $S_e(z)$. The properties of this function are characterized by 3 parameters: $\theta_{u\%,max}$ the limit MRS undetectable water content (when $S_e \to 0$), S_{lim} the threshold saturation above which MRS undetectable water content is constant, and $\theta_{u\%,base}$ the constant MRS undetectable water fraction for saturations higher than S_{lim} (Fig. 5).

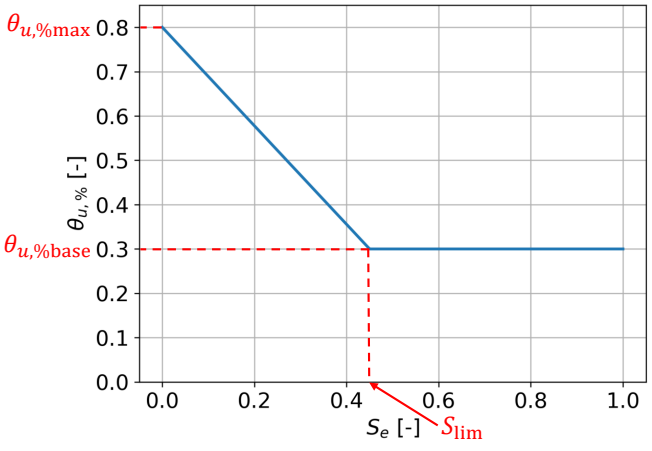

Figure 5. MRS undetectable water content: $\theta_{u\%}(S_e(z), \theta_{u\%,max}, S_{lim}, \theta_{u\%,base})$.

In this model, the effects of clay contents are taken into account by shifting the $\theta_{u\%,base}$ value (higher clay contents yield higher $\theta_{u\%,base}$). The effects of grain size distributions are modeled through both S_{lim} and $\theta_{u\%,base}$ (finer grains lead to lower S_{lim} values and the effects of the clay content are increased for coarse grains). To sum up the information presented in this section, we designed a flowchart of the hydrogeophysical model (Fig. 6).

https://doi.org/10.5194/egusphere-2026-3611
Preprint. Discussion started: 26 June 2026

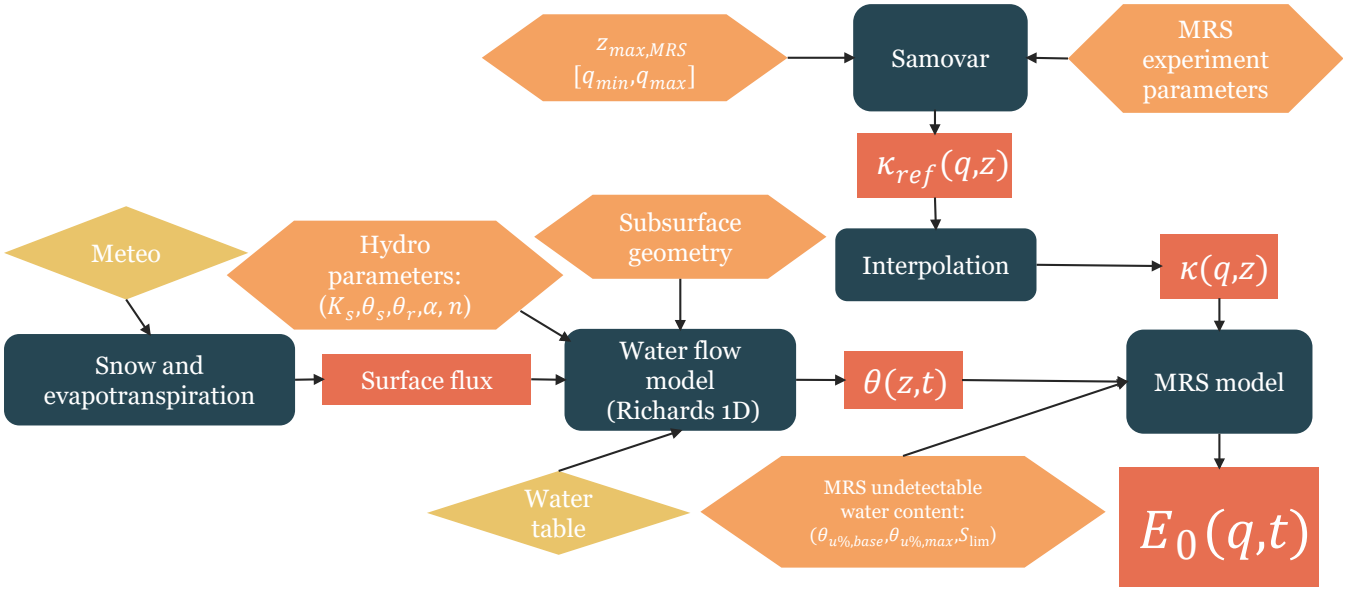

Figure 6. Flowchart of Phydrus-MRS hydrogeophysical modeling framework. Yellow diamond shaped boxes represent field data. Orange hexagons represent user defined parameters. Models and mathematical processings are shown as blue rectangles with rounded corners. Red rectangles represent the results of numerical models.

4 Global sensitivity analysis

4.1 Moment-based sensitivity indices

To perform a GSA of the MRS signals E_0 to variations of the hydrodynamic parameters, we used the moment-based sensitivity indices defined by Dell'Oca et al. (2017), for the first two statistical moments: AMAE and AMAV. We also used the classical variance-based sensitivity indices: Sobol indices (Sobol, 2001).

4.1.1 AMAE and AMAV indices

Let $y = f(\xi)$ be a mathematical model which input is a set of M independent random variables: $\xi = \{\xi_1, \xi_2, ..., \xi_M\}$. The AMA index associated with the first statistical moment (i.e. the mean), AMAE, quantifies the expected relative variation of the mean of y due to variations in ξ_i (Dell'Oca et al., 2017). For the second statistical moment (i.e. the variance), the AMAV index

https://doi.org/10.5194/egusphere-2026-3611
Preprint. Discussion started: 26 June 2026

quantifies the expected relative discrepancy between unconditional and conditional variance. The former is defined as:

$$AMAE_{\xi_i} = \begin{cases} \frac{E[|y_0 - E[y|\xi_i]|]}{|y_0|} & y_0 \neq 0, \\ E\left[|E\left[y|\xi_i\right]|\right] & y_0 = 0, \end{cases} \tag{11}$$

where $E[.|.]$ is the conditional expectation operator and y_0 is the unconditional expected value of y, and the latter is defined as:

$$AMAV_{\xi_i} = \frac{E\left[|V[y] - V\left[y|\xi_i\right]|\right]}{V[y]}, \tag{12}$$

where $V[.|.]$ is the conditional variance operator. These indices provide information that complements classical variance-based sensitivity measures. Using multiple sensitivity metrics makes our GSA approach more robust, as it does not rely on the assumption that the total influence of the hydrodynamic parameters can be fully captured through output variance alone. Furthermore, Dell'Oca et al. (2017) demonstrated that a given parameter may have a negligible Sobol index and still have an impact on the model output variance, quantified by the AMAV index. AMA-based GSA has been applied across diverse contexts, including hydrogeophysics (gravimetry, Maina and Guadagnini (2018)), risk assessment related to pesticide pollution (Tang et al., 2021), and land-surface modeling (Dell'Oca et al., 2025).

4.1.2 Sobol indices

Sobol (2001) shows that under the assumption that f is square-integrable, it can be uniquely decomposed in the following manner:

$$f(\xi) = y_0 + \sum_{i=1}^{M} f_i(\xi_i) + \sum_{j>i}^{M} f_{i,j}(\xi_i, \xi_j) + ... + f_{1...M}(\xi_1, ..., \xi_M), \tag{13}$$

where $f_{i_1,...,i_s}$ are centered orthogonal functions ($i_1, ..., i_s \subseteq \{1, ..., M\}$). This decomposition is called ANOVA, for ANalysis Of VAriance (Archer et al., 1997), because by squaring it and taking the mathematical expectation, one obtains a decomposition of the variance of $f(\xi)$:

$$V = \sum_{i=1}^{M} V_i + \sum_{j>i}^{M} V_{i,j} + ... + V_{1...M}, \tag{14}$$

where $V = var[f(\xi)]$ is the total variance of f, and $V_{i_1,...,i_s} = \text{var}\left[f_{i_1,...,i_s}\right]$ are the partial variances. Thanks to this decomposition, Sobol (2001) defines sensitivity indices, which measure the contribution of a model parameter to the output variance. The first Sobol index associated with the parameter ξ_i is:

$$S_{1,i} = \frac{\text{var}\left\{E\left[f(\xi)|\xi_i\right]\right\}}{\text{var}\left[f(\xi)\right]} = \frac{V_i}{V}. \tag{15}$$

https://doi.org/10.5194/egusphere-2026-3611
Preprint. Discussion started: 26 June 2026

Higher-order Sobol indices quantify the variance contributions of interactions among parameters:

$$S_{i_1,\ldots,i_s} = \frac{V_{i_1,\ldots,i_s}}{V}. \tag{16}$$

In this study, we compute and analyze the first and second order Sobol indices for the hydrodynamic parameters. Along with the AMA indices, these indices provide insights on the identifiability of ξ with observations of f. If a given parameter ξ_i has a negligible impact on the statistical moments of the function f, then observations of f will not help estimating the value of ξ_i (Wu et al., 2019). Sobol indices can be estimated with a Monte Carlo approach (Sobol, 2001). They can also be estimated with an approach based on Polynomial Chaos Expansion (PCE) (Sudret, 2008). The latter reduces the Sobol indices estimation problem to the estimation of the PCE coefficients, which is less expensive in terms of computing time than the original Monte Carlo approach.

4.2 Polynomial Chaos Expansion

PCE theory was originally developed by Wiener (1938). PCE is a class of surrogate models, widely used to replace process-based models in frameworks which require large numbers of model evaluations, such as GSA or Bayesian parameter inference (Sudret, 2008; Dell'Oca et al., 2017; Younes et al., 2018; Maina and Guadagnini, 2018; Rouzies et al., 2023). Under the assumption that the model function f is square integrable, it admits the following expansion (Soize and Ghanem, 2004):

$$f(\xi) = s_0\Psi_0 + \sum_{i=1}^{M} s_i\Psi_1(\xi_i) + \sum_{i<j}^{M} s_{i,j}\Psi_2(\xi_i,\xi_j) + \sum_{i<j<k}^{M} s_{i,j,k}\Psi_3(\xi_i,\xi_j,\xi_k) + \ldots \tag{17}$$

Let us consider the p^{th} order truncation of the series described in Eq. (17):

$$f(\xi) \approx \sum_{|\alpha|\leq p} s_\alpha \Psi_\alpha(\xi), \tag{18}$$

where $|\alpha| = \sum_{i=1}^{N} \alpha_i$, s_α are the polynomial coefficients, and Ψ_α are the α-degree polynomials of the orthogonal basis. The number of coefficients in this decomposition is

$$P + 1 = \frac{(M+p)!}{M!p!}. \tag{19}$$

The orthogonal polynomials corresponding to uniformly distributed random input parameters are Legendre polynomials (Sudret, 2008). Equation (18) is an ANOVA decomposition of f, as Ψ_α are orthogonal polynomials. Therefore, once the polynomial coefficients are estimated, one has direct access to Sobol indices through the definitions introduced in the previous section. We used the UQ[py]Lab python library to build the PCE and compute Sobol indices (Lataniotis et al., 2021).

https://doi.org/10.5194/egusphere-2026-3611
Preprint. Discussion started: 26 June 2026

In order to train the PCE surrogate models, we sampled 3000 realizations of the random vector containing the hydrogeophysical model parameters. We used the "Leave-One-Out" Cross-Validation (LOOCV) error ϵ_{LOO} to assess the quality of the PCE (Yates et al., 2023). LOOCV error is designed to avoid overfitting. N surrogate models $f^{PC/i}$ are created and trained on a reduced training set $X/x^i = \{x^j, j = 1, ..., N, j \neq i\}$. The cross-validation error is then computed by comparing the prediction of the model for the excluded sample $f^{PC/i}(x_i)$ with the real value $f(x_i)$. LOOCV error is defined as:

$$\epsilon_{LOO} = \frac{\Sigma_{i=1}^{N} \left(f(x_i) - f^{PC/i}(x_i)\right)^2}{\sum_{i=1}^{N} \left(f(x_i) - \hat{\mu}_Y\right)^2}, \tag{20}$$

where $\hat{\mu}_Y = \frac{1}{N} \sum_{i=1}^{N} f(x_i)$ is the empirical mean of the random samples model evaluation. PCE surrogate models reproduce with high accuracy the behavior of the forward model with a global maximum cross-validation error of $\epsilon_{LOO,max} = 1.1\ 10^{-2}$. This error reaches its maximum value for the second pulse $q_2 = 145$ A.ms. For pulses higher than $q2$ the cross-validation error decreases as the pulse value increases.

4.3 Experimental design

We consider a total number of 18 parameters in our GSA: the hydrodynamic parameters for the two subsurface layers $(\theta_{r,L}, \theta_{s,L}, \alpha_L, n_L, log_{10}(K_{s,L}))$ as well as the MRS undetectable water content function parameters $\theta_{u\%,base,L}$, $S_{lim,L}$, and $\theta_{u\%,max,L}$ ($L \in \{\text{soil}, \text{saprolite}\}$), the bedrock MRS water content $\theta_{MRS,bedrock}$, and Δh_{piezo} are considered as random variables following uniform distributions. The description of the parameters, and their variability ranges are summarized in Table 1. The ranges of Mualem-Van Genucthen parameters were chosen based on plausible estimates related to the Strengbach catchment (Hammecker et al., 2004). We chose $\log_{10}(K_s)$ $(-)$ as the random parameter (rather than K_s (m.s^{-1}) itself) because K_s varies by several orders of magnitude across soil types. We base the computation of Sobol indices on the coefficients of the PCE, and we produced 7000 additional simulations to compute AMAE and AMAV indices using Eq. (11) and Eq. (12).

https://doi.org/10.5194/egusphere-2026-3611
Preprint. Discussion started: 26 June 2026

Parameter	Description	Unit	Soil	Saprolite
$\log_{10}(K_s)$	$\log_{10}$ of saturated hydraulic conductivity	–	$[-6.56, -3.38]$	$[-6.56, -5.38]$
θ_r	residual water content	–	$[0.00, 0.10]$	$[0.00, 0.04]$
θ_s	saturated water content	–	$[0.30, 0.50]$	$[0.08, 0.20]$
n	VG parameter	–	$[1.1, 3.0]$	$[1.1, 3.0]$
α	VG parameter	m^{-1}	$[1.0, 15.0]$	$[1.0, 15.0]$
$\theta_{u\%,base}$	base $\theta_{u\%}$ value	–	$[0.20, 0.45]$	$[0.20, 0.45]$
S_{lim}	limit saturation threshold	–	$[0.40, 0.50]$	$[0.40, 0.50]$
$\theta_{u\%,max}$	maximum $\theta_{u\%}$ value	–	$[0.50, 0.70]$	$[0.50, 0.70]$
Other Parameters				
Δh_{piezo}	piezometric uncertainty	m	$[-0.20, 0.20]$	
$\theta_{MRS,bedrock}$	bedrock MRS water content	–	$[0.01, 0.05]$	

Table 1. Ranges of variability of the hydrogeophysical model parameters. All parameters follow uniform distributions on the intervals $[min, max]$.

A straightforward and global approach to assess the dataset we produced by sampling the parameter space detailed in Table 1 is to estimate and visualize the pdfs of the MRS signals E_0 simulated from these samples. The pdfs are estimated with the gaussian kernel density estimator tool of the Scipy python library (Virtanen et al., 2020). We estimated these pdfs at five key moments of the period considered in the numerical experiment: the initial state ($t = 0$ d), during the rain event and the rising phase of the water table ($t = 5$ d), at the end of this phase ($t = 10$ d), and at two later times ($t = 30$ d and $t = 50$ d) after the water table returned to its initial depth.

5 Results

5.1 E_0 probability density functions

We estimated the pdfs of the MRS signals at simulation times $t \in \{0, 5, 10, 30, 50\}$ days for the five pulse values ($E_0(q_i), i \in \{1, ..., 5\}$). The signal pdfs for the fifth pulse behave similarly to those of the fourth pulse. Therefore, we only present here the results concerning the first four pulse values (Fig. 7). We show the corresponding results for q_5 on Fig. S1 in the Supplement.

https://doi.org/10.5194/egusphere-2026-3611
Preprint. Discussion started: 26 June 2026

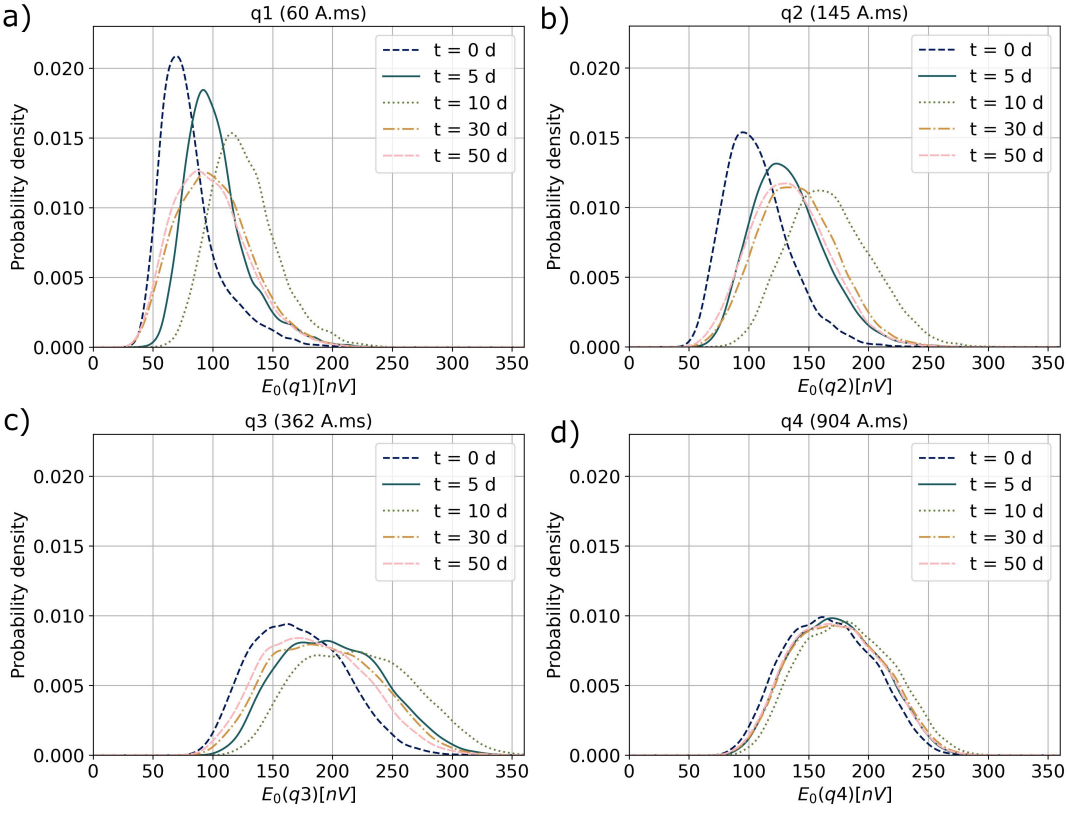

Figure 7. MRS signal $E_0(q_i)$ probability density functions at times $t \in \{0, 5, 10, 30, 50\}$ days for increasing pulse values: a) $q_1 = 60$ A.ms, b) $q_2 = 145$ A.ms, c) $q_3 = 362$ A.ms, d) $q_4 = 904$ A.ms.

We observe a shift in the pdfs of the MRS signals towards higher values between day zero and day ten (Fig. 7a to d). This indicates that during the first ten days of the simulation period, the mean value of MRS signals increases. For the five pulse values at times $t = 30$ d and $t = 50$ d, the pdfs exhibit similar shapes. The distributions widen (i.e. show higher variance) as the pulse value increases from q_1 (Fig. 7a) to q_3 (Fig. 7c). The distributions for q_4 (Fig. 7d) are slightly narrower than those for q_3. They also show the weakest temporal variations: the pdf curves are almost superimposed at all examined times. We make the same observations for q_5, which also displays narrower distributions centered on lower signal values (Fig. S1 in the Supplement). The pdfs also display an asymmetry, with a higher probability for stronger MRS signals. This asymmetry is more important for the lower pulse values and at earlier simulation times.

5.2 Global sensitivity indices: q_1

The global sensitivity indices presented in Sect. 4 exhibit their strongest temporal variability and the largest contrasts between AMAE, AMAV, and S_1 for the first pulse moment ($q_1 = 60$ A.ms; Fig. 8). Over the entire simulated period, n_{soil} exerts the dominant control on both the mean and variance of the MRS signals. After approximately 12-17 days, depending on the sen-

https://doi.org/10.5194/egusphere-2026-3611
Preprint. Discussion started: 26 June 2026

sitivity index considered, $K_{s,soil}$ emerges as the second most influential parameter. During the early stage of the numerical experiment, $\theta_{r,soil}$ significantly affects both the mean and variance of the MRS signals (Fig. 8a,c), but its influence decreases rapidly thereafter. The most pronounced differences among sensitivity indices are observed for the AMAV metric: AMAV values associated with $\theta_{s,soil}$ and $\theta_{u\%,base,soil}$ remain high (approximately 0.20) throughout the simulation, indicating a persistent contribution of these parameters to the variance of the MRS signals. In contrast, AMAE and S_1 identify $\theta_{s,sapro}$ as the third most influential parameter. Despite these differences, all three sensitivity indices show similar temporal patterns for n_{soil}, with a sharp decline during the first 13 days followed by a renewed increase, more pronounced for the mean response (AMAE; Fig. 8a) than for the variance (AMAV and S_1; Fig. 8b,c). Sensitivity indices associated with $K_{s,soil}$ increase rapidly during the first 20 days before stabilizing, whereas those related to $\theta_{r,soil}$ display an opposite trend over the same period. Finally, sensitivity indices for the remaining influential parameters ($\theta_{s,sapro}$ for AMAE and S_1; $\theta_{s,soil}$ and $\theta_{u\%,base,soil}$ for AMAV) exhibit weaker temporal variability and remain close to their initial values throughout the experiment.

https://doi.org/10.5194/egusphere-2026-3611
Preprint. Discussion started: 26 June 2026

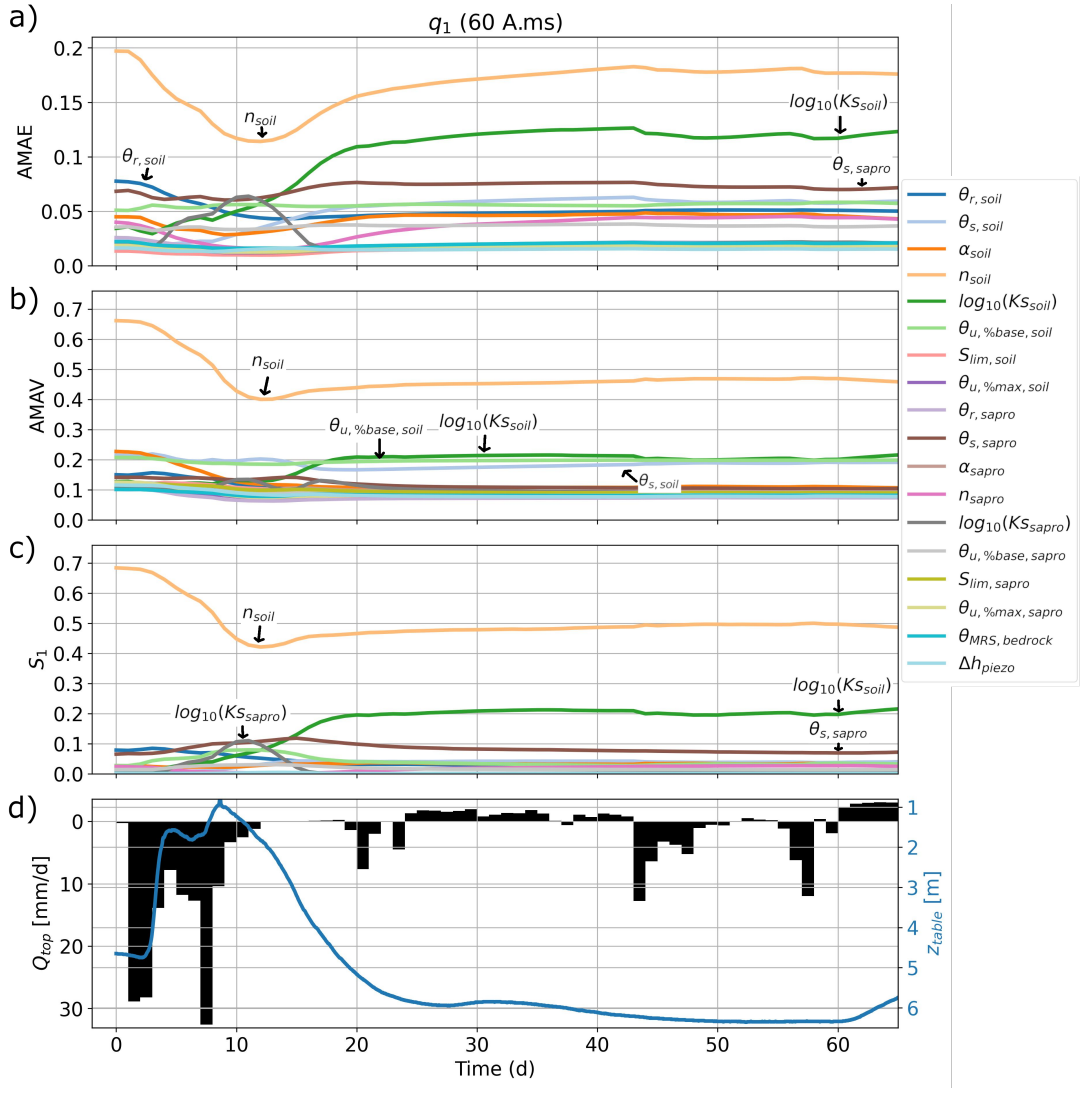

Figure 8. Time series of a) AMAE, b) AMAV and c) S_1 sensitivity indices of MRS signals for the first pulse value: $q1 = 60.0$ A.ms, and d) time-series of the data constraining the model BC: upper BC (black) and bottom BC (blue).

5.3 Global sensitivity indices: q_2 to q_5

For higher pulse values ($q_2 = 145$ A.ms to $q_4 = 904$ A.ms), the sensitivity indices related to the variance of the MRS signals (AMAV and S_1) exhibit similar behaviors. Therefore, we describe and analyze only the AMAE and S_1 indices and their temporal dynamics for these pulse values (Fig. 9). The time series of AMAV indices for pulses q_1 to q_5 are provided in Fig. S2 in the Supplement. For the fifth pulse, the mean and variance of the MRS signals are largely controlled by a single parameter, $\theta_{MRS,bedrock}$, and the corresponding sensitivity indices remain constant throughout the simulated period (Fig. S3 in the Supplement).

https://doi.org/10.5194/egusphere-2026-3611
Preprint. Discussion started: 26 June 2026

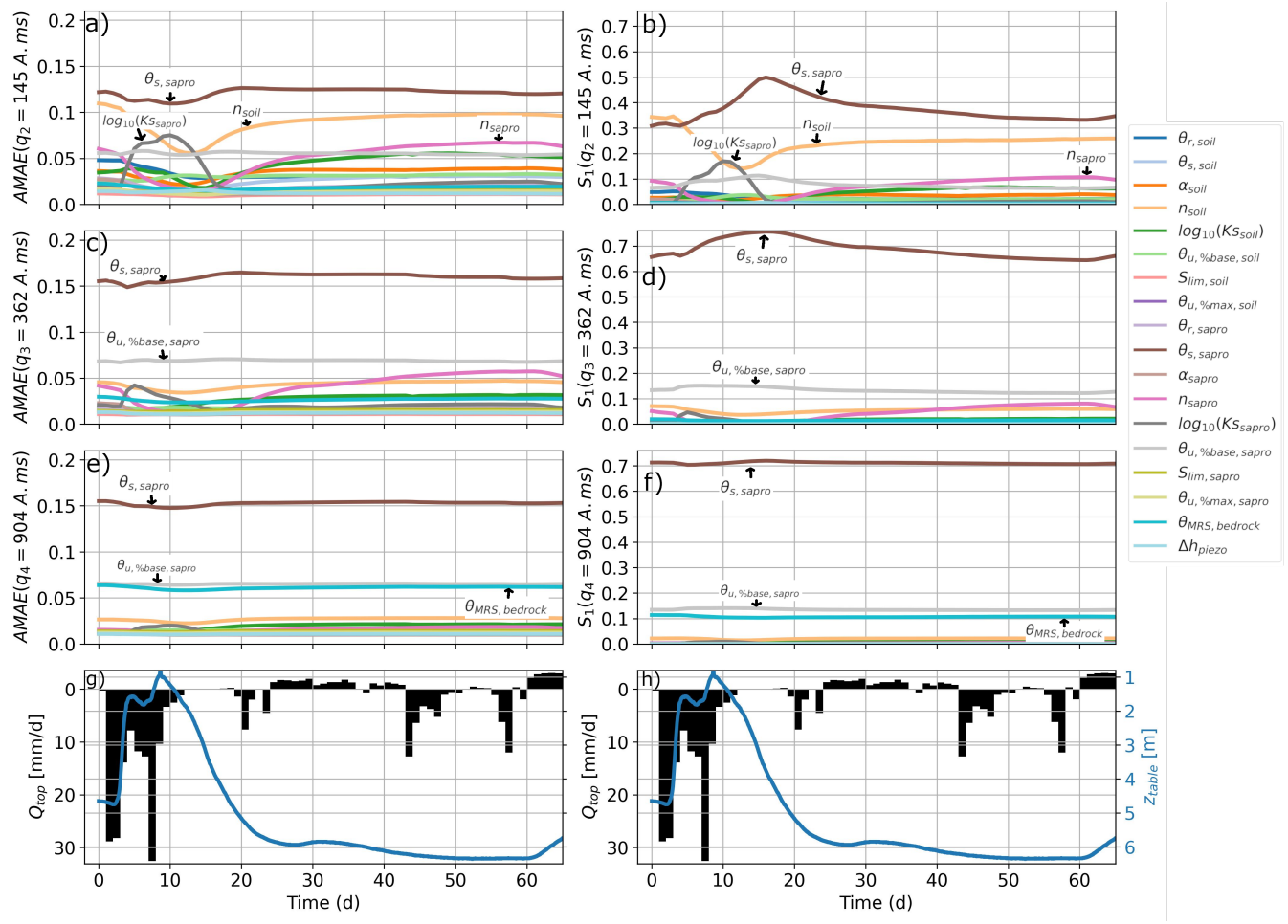

Figure 9. Time series of AMAE (left column: a, c, e) and S_1 (right column: b, d, f) for q2, q3 and q4, and time-series of the data constraining the model BC: upper BC (black) and bottom BC (blue) (g, h).

$\theta_{s,sapro}$ exerts the strongest influence on both the mean and variance of the MRS signals for pulses q_2 to q_4. For the second pulse, n_{soil} also remains influential (Fig. 9a,b): it is the second most influential parameter for most of the simulated period and the main driver of variance during the first days. Sensitivity to $K_{s,sapro}$ shows pronounced temporal variability between days three and 17 (Fig. 9a,b). It increases markedly until day ten, when it reaches a maximum and $K_{s,sapro}$ temporarily becomes the second most influential parameter. After day ten, sensitivity to $K_{s,sapro}$ decreases back to its initial level. Sensitivity indices associated with n_{sapro} display opposite dynamics: they are initially significant, decrease between days three and 17, and then return close to their initial values for q_2 (Fig. 9a,b), while continuing to increase for q_3 (Fig. 9c,d). $\theta_{u\%,base,sapro}$ also has a major contribution to both the mean and variance of the MRS signals for pulses q_3 and q_4. The variability of $\theta_{MRS,bedrock}$ is significant only for the higher pulse values (q_4 and q_5). In contrast, the VG parameters α and θ_r in the saprolite zone have a negligible effect on the mean and variance of the MRS signals at all times and for all pulse values. The same conclusion applies

https://doi.org/10.5194/egusphere-2026-3611
Preprint. Discussion started: 26 June 2026

to two parameters related to the MRS-undetectable water content, S_{lim} and $\theta_{u\%,max}$, in both the soil and saprolite zones, and to Δh_{piezo}. Table 2 summarizes the sensitivity of the MRS signals to hydrodynamic parameters for all pulse values and for the three sensitivity indices considered.

	q1			q2			q3			q4			q5		
Parameter	AMAE	AMAV	S_1	AMAE	AMAV	S_1	AMAE	AMAV	S_1	AMAE	AMAV	S_1	AMAE	AMAV	S_1
$\theta_{r,soil}$	+∼	-	+∼	+∼	-	-	-	-	-	-	-	-	-	-	-
$\theta_{s,soil}$	-	+_	-	-	-	-	-	-	-	-	-	-	-	-	-
α_{soil}	-	+∼	-	-	-	-	-	-	-	-	-	-	-	-	-
n_{soil}	+++∼	+++∼	+++∼	++∼	++∼	++∼	+_	-	+_	-	-	-	-	-	-
$\log_{10}(K_{s,soil})$	++∼	+∼	++∼	+∼	-	-	-	-	-	-	-	-	-	-	-
$\theta_{u\%,base,soil}$	-	+_	+∼	-	-	-	-	-	-	-	-	-	-	-	-
$S_{lim,soil}$	-	-	-	-	-	-	-	-	-	-	-	-	-	-	-
$\theta_{u\%,max,soil}$	-	-	-	-	-	-	-	-	-	-	-	-	-	-	-
$\theta_{r,sapro}$	-	-	-	-	-	-	-	-	-	-	-	-	-	-	-
$\theta_{s,sapro}$	+_	-	+_	++_	++∼	++∼	+++_	+++∼	+++∼	+++_	+++_	+++_	+_	-	-
α_{sapro}	-	-	-	-	-	-	-	-	-	-	-	-	-	-	-
n_{sapro}	-	-	-	+∼	-	+∼	+∼	+∼	+∼	-	-	-	-	-	-
$\log_{10}(K_{s,sapro})$	+∼	-	-	++∼	-	++∼	+∼	-	-	-	-	-	-	-	-
$\theta_{u\%,base,sapro}$	-	-	-	+_	-	+_	++_	++_	++_	+_	+_	+_	-	-	-
$S_{lim,sapro}$	-	-	-	-	-	-	-	-	-	-	-	-	-	-	-
$\theta_{u\%,max,sapro}$	-	-	-	-	-	-	-	-	-	-	-	-	-	-	-
$\theta_{MRS,bedrock}$	-	-	-	-	-	-	-	-	-	++_	++_	++_	+++_	+++_	+++_
Δh_{piezo}	-	-	-	-	-	-	-	-	-	-	-	-	-	-	-

Table 2. Summary of the sensitivity of the MRS signals to the hydrodynamic parameters. The symbol "+" denotes significant sensitivity, whereas "–" indicates negligible sensitivity. For parameters exhibiting significant sensitivity, we further indicate whether sensitivity varies over time (denoted by "∼") or remains stable throughout the numerical experiment (denoted by "_").

5.4 Parameters interactions

The presented sensitivity indices account for the independent effects of the hydrodynamic parameters. Higher-order indices should be computed in order to take into account the interactions between parameters. The magnitude of these interactions can be estimated by summing the first-order Sobol indices of all the parameters (Fig. 10). The greater the difference between this sum and unity is, the stronger the interactions between the parameters are.

https://doi.org/10.5194/egusphere-2026-3611
Preprint. Discussion started: 26 June 2026

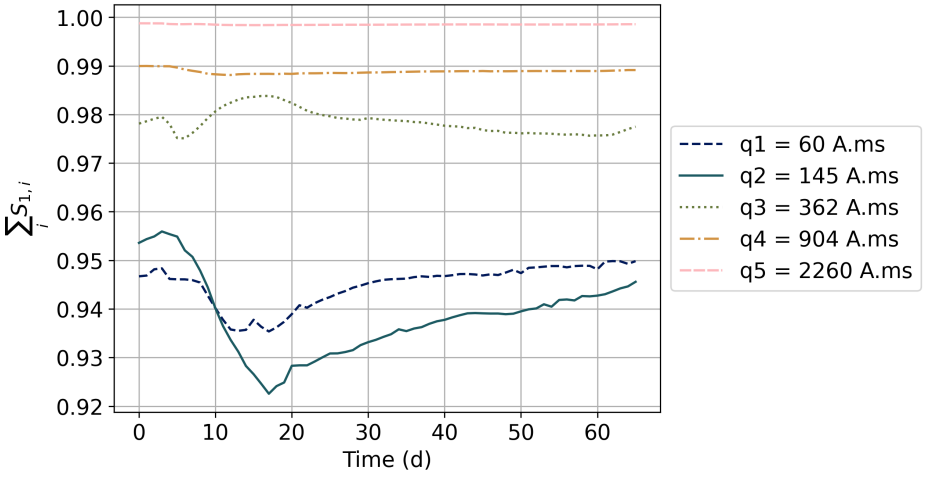

Figure 10. Time series of the sum of all the first order Sobol indices $\sum_i S_{1,i}$ for the five pulse values.

For the highest pulse values, nearly all of the variance can be explained by independent effects of the model parameters (Fig. 10). The interactions are stronger for q_1 and q_2: up to more than 6% and 7% of the variance can be attributed to the interaction between parameters for q_1 and q_2, respectively. Investigation of the second-order Sobol indices shows that the couples of parameters all have a second order index smaller than 0.02, indicating that the difference between the sum of first order Sobol indices and unity is composed of multiple weak interactions.

6 Discussions

6.1 E_0 probability density functions

The increase in the mean amplitude of the MRS signals for all pulses during the first ten days of the numerical experiment (observed in Fig. 7) is a direct consequence of the meteorological event. Indeed, surface infiltration and the rise in the water table level lead to stronger MRS signals. On the other hand, the evolution of variance with increasing pulses reflects the investigation depths associated with the different pulses. From q_1 to q_3, the variance increases as the signals become progressively sensitive to deeper regions (Fig. 4) which exhibit a higher degree of saturation (see Fig. S4 in the Supplement). Pulses q_4 and q_5 are primarily sensitive to the portion of the subsurface column that is always saturated. However, the variance is slightly lower for q_4 due to lower values of the sensitivity function κ (Fig. 4). It is smaller for q_5, because of both lower values of the sensitivity function and the narrower variation range for the water content in the bedrock layer (Sect. 4.3). The MRS signals pdfs indicate a satisfactory sampling of the parameter space. The superposition of the pdfs corresponding to similar hydric states at $t = 30$ and $t = 50$ d (see Fig. S4 in the Supplement for the mean saturation distributions) confirms that the parameter space was explored with a sufficient number of Monte Carlo realizations. For all considered pulses and at all simulation times,

https://doi.org/10.5194/egusphere-2026-3611
Preprint. Discussion started: 26 June 2026

the pdfs of MRS signals do not display multimodality. Furthermore, the observed asymmetry is low to moderate. This ensures the relevance of variance-based sensitivity analysis (Saltelli et al., 2002).

6.2 GSA for q_1

For the first pulse value, the parameter which has the strongest influence on both the mean and variance of the MRS signals is n_{soil}. This dominant effect arises from the strong influence of n on the relationship between pressure h and water content θ (Eq. 2), especially in the low saturation domain ($h < 0$ with high absolute value). The parameter α also affects this relationship, but to a lesser extent, which explains the difference in how these two parameters impact the MRS signals (see Fig. S5 in the Suppelement, showing retention curves $\theta(h)$ for several values of n and α). During the meteorological event (rainfall infiltration and water table rise), sensitivity to n_{soil} decreases, whereas sensitivity to $K_{s,soil}$ increases (Fig. 8). Sensitivity to n_{soil} stops decreasing once the rain event ends (after day 12), indicating that the primary driver of this sensitivity is the surface infiltration flux Q_{top}, and that this flux negatively affects the influence of n_{soil}. In contrast, sensitivity to $K_{s,soil}$ stabilizes a few days after the end of the infiltration event. This delay may result from the presence of an infiltration front, whose propagation speed is controlled by $K_{s,soil}$ through its effect on the (unsaturated) hydraulic conductivity (Eq. 3).

The values of the AMAV index for the parameters $\theta_{u\%,base,soil}$ and $\theta_{s,soil}$ (Fig. 8b) imply that these two parameters have a non-negligible impact on the variance of the MRS signals. This observation highlights the relevance of using multiple sensitivity measures. Indeed, basing our GSA approach on S_1 solely would have led us to the wrong conclusion that the two aforementioned parameters do not have an impact on the variance of MRS signals. This is consistent with the results by Dell'Oca et al. (2017), who showed for an analytical benchmark function that the Sobol indices can miss the effects of some parameters on the outputs of a model.

We also observe a different baseline value for the indices AMAE, AMAV and S_1. This baseline value provides information on the precision of the estimation of the sensitivity indices. Only the parameters with sensitivity indices above this baseline can be discussed with confidence. The baseline value for the AMAE indices is around 0.025, that for the AMAV indices is close to 0.10. Despite this fact, the sensitivities discussed so far lie above this baseline. The Sobol indices are estimated with a better precision as their baseline is close to zero. This may be due to the high accuracy of the PCE used to compute the Sobol indices.

6.3 GSA for q_2 to q_4

The consistently strong influence of $\theta_{s,sapro}$ on both the variance and the mean of the MRS signals for pulses q_2 to q_4 can be explained by the fact that a non-negligible fraction of the saprolite zone remains permanently saturated. Under saturated conditions, the water content θ (and, consequently, the MRS signals) is solely controlled by the parameter θ_s (Eq. 2). For pulses q_3 and q_4, the parameter $\theta_{u\%,base,sapro}$ has a strong and constant influence on both the mean and the variance of the MRS signals. This results from the high degree of saturation in the regions of sensitivity of these two pulses. These saturation values are consistently above the saturation threshold S_{lim}, making $\theta_{u\%,base,sapro}$ the only parameter influencing the MRS undetectable water content (Fig. 5).

https://doi.org/10.5194/egusphere-2026-3611
Preprint. Discussion started: 26 June 2026

Whereas the second pulse remains sensitive to some of the soil hydrodynamic parameters, higher pulse values are primarily sensitive to the saprolite zone parameters. The variability of the parameter n_{sapro} is significant for pulses q_2 and q_3 during periods when the water table level is low. The temporal dynamics of the sensitivity indices for pulse q_2 are largely governed by the bottom boundary condition. For instance, the sensitivity indices associated with $K_{s,sapro}$ exhibit the same temporal trend as the water table level during the meteorological event. Sensitivity to $\theta_{s,sapro}$ is correlated with the rise of the water table, but displays a temporal delay. This delay arises from the two dynamics driving the system: (1) the propagation of the precipitation infiltration front, and (2) the rise of the water table. Analysis of water content distributions from individual simulations (see Fig. S6 in the Supplement) shows that, depending on the parameter set, the infiltration front reaches the saturated zone at different times. In some simulations, this introduces a delay in when the top of the saturated zone reaches its lowest depth. Finally, the sensitivity dynamics become less pronounced as the pulse value increases, consistent with the analysis of the pdfs of the MRS signals.

6.4 Parameters with insignificant contribution

Some parameters have a negligible impact on both the mean and variance of MRS signals for all pulse values and at all times. Among these parameters are two of VG parameters related to the saprolite layer: $\theta_{r,sapro}$ and α_{sapro}. These parameters have a negligible impact on the MRS signals because they do not affect the water content in the saturated part of the subsurface column. Concerning the MRS undetectable water content fraction, two of the three parameters governing this quantity always exhibit a negligible impact: $\theta_{u\%,max}$ and S_{lim}. $\theta_{u\%,max}$ is the limit fraction of undetectable water content when the saturation tends to zero (Fig. 5). Although the fraction of undetectable water increases with decreasing saturation, the value of $\theta_{u\%,max}$ does not appear to influence the MRS signals. This is likely because it primarily affects the lowest saturation values, which contribute only weakly to the MRS signals. Furthermore, the water content distributions show very sharp transitions in saturation (Fig. S6 in the Supplement). As a result, the position of the threshold S_{lim} along the saturation axis is of minor importance, since saturation rapidly transitions from values above the threshold to values that are negligible for the MRS response over very short depth intervals. Regarding parameter identifiability, our results indicate that under the investigated experimental conditions, these six parameters - namely $\theta_{r,sapro}$, α_{sapro}, S_{lim}, and $\theta_{u\%,max}$ in both the soil and saprolite zones - are unlikely to be accurately estimated through an inverse problem based solely on time-lapse MRS data (Wu et al., 2019). This limitation could be mitigated by incorporating complementary data into the inversion framework. Useful constraints include direct water content measurements (Belfort et al., 2018) or supplementary geophysical datasets, such as seismic and gravimetric data (Fores et al., 2018) or ERT and self-potential data (Li et al., 2024). Additionally, integrating GPR with time-lapse MRS data holds significant potential; the shallow depth of investigation characteristic of GPR would effectively complement the deeper sensitivity of MRS measurements (Legchenko et al., 2018).

To maintain a focused GSA, the framework excludes the effects of environmental electromagnetic noise on MRS data. Because such noise introduces a random bias independent of subsurface hydrodynamic processes, it is expected to globally attenuate parameter identifiability rather than alter the relative sensitivity of individual parameters.

https://doi.org/10.5194/egusphere-2026-3611
Preprint. Discussion started: 26 June 2026

The parameter Δh_{piezo}, introduced to account for the uncertainty in the representativity of the piezometric data for the studied area, also has a negligible impact on both the variance and the mean of MRS signals for all pulse values. This result suggests that, assuming the uncertainty in the representativity of the piezometric measurements varies within the range $[-0.20, 0.20]$ m, it does not have a measurable impact on the MRS signal statistical moments. Finally, the sum of first-order Sobol indices is always close to unity, indicating that parameter interactions have a negligible contribution to the variance of the MRS signals.

7 Conclusions

We present a hydrogeophysical model, coupling the one-dimensional Richards equation for subsurface unsaturated water flow with the geophysical method of MRS. We analyze the sensitivity of MRS signals to hydrodynamic parameters and uncertainties in the lower BC in the context of a meteorological event which occurred in winter 2021 in the Strengbach headwater catchment. During this intense meteorological event, a fast saturation of the underground porous medium was observed due to the combined effect of snowmelt (0.8 m of snow accumulated before the event) and a strong and long lasting rain event (107 mm cumulated over a period of 12 days). To conduct the GSA, we designed a numerical experiment based on real hydrological and meteorological data collected at the Strengbach catchment. This numerical experiment allows us to simulate signal acquisition for several pulse moments as if they could be acquired simultaneously and to explore acquisitions repeated through time every 24 hours. The domain geometry, parameters and boundary conditions are representative of the studied site. Following the conclusions of Dell'Oca et al. (2017), we used several sensitivity indices to quantify the effects of uncertainty in hydrodynamic parameters on the MRS signals. We conducted the sensitivity analysis with the classical variance-based Sobol indices, together with the AMAE and AMAV indices. Thus, we present a robust GSA of the hydrogeophysical model, free from the assumption that the totality of the effects of hydrodynamic parameters can be captured solely through their impact on the model output variance. To the best of our knowledge, the model we developed for this study is the first one to account for the fraction of MRS-undetectable water content within the modeling framework thereby enabling simulation of MRS signals of the same order of magnitude as typical experimental observations using realistic hydrodynamic parameters for the soil and saprolite zones. The results of the numerical experiment lead to the following conclusions:

1. The parameters which exert the strongest influence on the mean and variance of the MRS signals depend on the pulse value. For the lowest pulse value (i.e., the shallowest depth of investigation), the dominant parameter controlling both the mean and variance of MRS signals is the VG parameter n in the soil layer, followed by $K_{s,\mathrm{soil}}$. For pulses q_2 to q_4, the most influential parameter is θ_s in the saprolite zone. n_{soil}, $K_{s,sapro}$ and n_{sapro} have significant contributions to the MRS signals mean and variance of the second pulse. For the third and fourth pulse, the second most influential parameters are $\theta_{u\%,base,sapro}$ and $\theta_{MRS,bedrock}$ respectively. Finally, the dominant parameter associated with the fifth pulse (i.e. the deepest region of investigation) is the MRS water content in the bedrock zone.

2. Some parameters have a negligible impact on both the mean and variance of the MRS signals across all times and pulse values. Among the subsurface flow parameters, the non-sensitive ones are $\theta_{r,sapro}$ and α_{sapro}. For the parameters related

https://doi.org/10.5194/egusphere-2026-3611
Preprint. Discussion started: 26 June 2026

to the MRS-undetectable water content fraction, the parameters with negligible influence on MRS signals are $\theta_{u\%,max}$ and S_{lim} (in both the soil and saprolite zone). Consequently, these six parameters are unlikely to be accurately estimated from an inverse problem relying solely on time-lapse MRS data.

3. The use of multiple sensitivity indices provides valuable information beyond that obtained from a Sobol-indices-only GSA. Indeed, it prevents the erroneous conclusion that the parameters $\theta_{s,soil}$ and $\theta_{u\%,base,soil}$ have a negligible impact on the MRS signals for the first pulse value.

4. The temporal dynamics of the sensitivity indices of MRS signals are stronger for lower pulse values. We conclude that these pulse values are the most relevant to repeat in a time-lapse experiment. In this context, energy can be saved by avoiding repetition of the highest pulse values which are also the most energy-intensive, and by focusing on lower pulse values for investigating the shallow subsurface. However, this conclusion is site dependent and a dedicated sensitivity analysis can help defining the most appropriate MRS acquisition sequence in other settings.

The results of this study provide valuable insights for estimating hydrodynamic parameters from time-lapse MRS data and for guiding the design of future experimental developments.While this study leverages site-specific geological data and a distinct meteorological event, the integrated GSA framework provides a transferable methodology applicable to geophysical monitoring experiments across diverse hydrogeological contexts. The GSA results constitute a solid comprehension basis of the model's behavior, which is a crucial information before attempting subsurface flow model calibration with time-lapse MRS data.

Code and data availability. The meteorological data and the water table depth measured in the piezometer pz5b used to compute the boundary conditions were obtained from the OHGE database (https://bd-ohge.unistra.fr/OHGE/). This database is accessible upon creation of an account and request of access. The transformed data (computed boundary conditions), the hydrodynamic parameters samples, the simulated MRS signals and the codes implementing the Phydrus-MRS forward model, the GSA of the model and the visualization routines are available on Zenodo (Gru et al., 2026) (https://doi.org/10.5281/zenodo.20558903). The routines used to define the PCE metamodels and compute the Sobol sensitivity indices are available in the UQ[py]Lab python library (Lataniotis et al., 2021). The Phydrus python library used for unsaturated water flow simulation (Collenteur et al., 2020) is publicly available.

Author contributions. GG: Conceptualization, Data curation, Formal analysis, Investigation, Methodology, Software, Validation, Visualization, Writing (original draft preparation, review and editing), JFG: Conceptualization, Supervision, Writing (review and editing), PA: Conceptualization, Supervision, Software, Writing (review and editing), NL : Conceptualization, Funding acquisition, Project administration, Supervision, Writing (review and editing)

Competing interests. Some authors are members of the editorial board of the journal HESS.

https://doi.org/10.5194/egusphere-2026-3611
Preprint. Discussion started: 26 June 2026

Acknowledgements. The authors acknowledge financial support from the University of Strasbourg, which funded the PhD fellowship of Guillaume Gru, the institut des Mathématiques pour la Planète Terre (iMPT), and the French National Research Agency (ANR) through the CASH project (ANR-24-CE56-3383-01). The authors would further like to thank Solenn Cotel for providing her expertise on the field of study and Benjamin Belfort for the help in the modeling of the surface infiltration flux.

https://doi.org/10.5194/egusphere-2026-3611
Preprint. Discussion started: 26 June 2026

References

Archer, G. E. B., Saltelli, A., and Sobol, I. M.: Sensitivity measures,anova-like Techniques and the use of bootstrap, Journal of Statistical Computation and Simulation, 58, 99–120, https://doi.org/10.1080/00949659708811825, 1997.

Beaulieu, E., Lucas, Y., Viville, D., Chabaux, F., Ackerer, P., Goddéris, Y., and Pierret, M.-C.: Hydrological and vegetation response to climate change in a forested mountainous catchment, Modeling Earth Systems and Environment, 2, 1–15, https://doi.org/10.1007/s40808-016-0244-1, 2016.

Belfort, B., Toloni, I., Ackerer, P., Cotel, S., Viville, D., and Lehmann, F.: Vadose Zone Modeling in a Small Forested Catchment: Impact of Water Pressure Head Sampling Frequency on 1D-Model Calibration, Geosciences, 8, 72, https://doi.org/10.3390/geosciences8020072, 2018.

Belfort, B., Alzein, A., Cotel, S., Julien, A., and Weill, S.: Hydrodynamic Parameter Estimation for Simulating Soil-Vegetation-Atmosphere Hydrology Across Forest Stands in the Strengbach Catchment, Hydrology, 13, 11, https://doi.org/10.3390/hydrology13010011, 2025.

Benton, J. R., McGuire, K. J., and Schreiber, M. E.: Subsurface permeability contrasts control shallow groundwater flow dynamics in the critical zone of a glaciated, headwater catchment, Hydrological Processes, 36, https://doi.org/10.1002/hyp.14672, 2022.

Binley, A., Hubbard, S. S., Huisman, J. A., Revil, A., Robinson, D. A., Singha, K., and Slater, L. D.: The emergence of hydro-geophysics for improved understanding of subsurface processes over multiple scales, Water Resources Research, 51, 3837–3866, https://doi.org/10.1002/2015wr017016, 2015.

Boucher, M., Costabel, S., and Yaramanci, U.: The detectability of water by NMR considering the instrumental dead time – a laboratory analysis of unconsolidated materials, Near Surface Geophysics, 9, 145–154, https://doi.org/https://doi.org/10.3997/1873-0604.2010056, 2011.

Boucher, M., Pierret, M.-C., Dumont, M., Viville, D., Legchenko, A., Chevalier, A., and Penz, S.: MRS characterisation of a mountain hard rock aquifer: the Strengbach Catchment, Vosges Massif, France, in: MRS 2015/6th international workshop on Magnetic Resonance Sounding, 2015.

Chaffaut, Q., Lesparre, N., Masson, F., Hinderer, J., Viville, D., Bernard, J.-D., Ferhat, G., and Cotel, S.: Hybrid gravimetry to map water storage dynamics in a mountain catchment, Frontiers in Water, 3, 715 298, https://doi.org/10.3389/frwa.2021.715298, 2022.

Collenteur, R., Vremec, M., and Brunetti, G.: Interfacing FORTAN Code with Python: an example for the Hydrus-1D model, https://doi.org/10.5194/egusphere-egu2020-15377, 2020.

Costabel, S. and Günther, T.: Noninvasive Estimation of Water Retention Parameters by Observing the Capillary Fringe with Magnetic Resonance Sounding, Vadose Zone Journal, 13, 1–14, https://doi.org/10.2136/vzj2013.09.0163, 2014.

Dell'Oca, A., Riva, M., and Guadagnini, A.: Moment-based metrics for global sensitivity analysis of hydrological systems, Hydrology and Earth System Sciences, 21, 6219–6234, https://doi.org/10.5194/hess-21-6219-2017, 2017.

Dell'Oca, A., Luttenauer, D., Guadagnini, A., Weill, S., and Ackerer, P.: Relative importance of uncertain model parameters driving water fluxes in a land surface model, Journal of Hydrology, 663, 134 310, https://doi.org/10.1016/j.jhydrol.2025.134310, 2025.

Ebel, B. A. and Loague, K.: Physics-based hydrologic-response simulation: Seeing through the fog of equifinality, Hydrological Processes, 20, 2887–2900, https://doi.org/10.1002/hyp.6388, 2006.

Ferretti, F., Saltelli, A., and Tarantola, S.: Trends in sensitivity analysis practice in the last decade, Science of The Total Environment, 568, 666–670, https://doi.org/10.1016/j.scitotenv.2016.02.133, 2016.

https://doi.org/10.5194/egusphere-2026-3611
Preprint. Discussion started: 26 June 2026

Fichter, J., Dambrine, E., Turpault, M.-P., and Ranger, J.: Base cation supply in spruce and beech ecosystems of the Strengbach catchment (Vosges mountains, NE France), Water, Air, and Soil Pollution, 104, 125–148, https://doi.org/10.1023/a:1004966302517, 1998.

Fores, B., Champollion, C., Mainsant, G., Albaric, J., and Fort, A.: Monitoring Saturation Changes with Ambient Seismic Noise and Gravimetry in a Karst Environment, Vadose Zone Journal, 17, 1–12, https://doi.org/10.2136/vzj2017.09.0163, 2018.

Gilding, B.: Qualitative mathematical analysis of the Richards equation, Transport in Porous Media, 6, https://doi.org/10.1007/bf00137854, 1991.

Granier, A., Bréda, N., Biron, P., and Villette, S.: A lumped water balance model to evaluate duration and intensity of drought constraints in forest stands, Ecological Modelling, 116, 269–283, https://doi.org/10.1016/s0304-3800(98)00205-1, 1999.

Gru, G., Girard, J.-F., Ackerer, P., and Lesparre, N.: Codes and data for the paper Sensitivity of time- lapse magnetic resonance sounding to vadose zone hydrodynamic parameters: monitoring of an intense meteorological event, https://doi.org/10.5281/zenodo.20558903, 2026.

Grêt-Regamey, A. and Weibel, B.: Global assessment of mountain ecosystem services using earth observation data, Ecosystem Services, 46, 101 213, https://doi.org/10.1016/j.ecoser.2020.101213, 2020.

Hammecker, C., Barbiéro, L., Boivin, P., Maeght, J. L., and Diaw, E. H. B.: A Geometrical Pore Model for Estimating the Microscopical Pore Geometry of Soil with Infiltration Measurements, Transport in Porous Media, 54, 193–219, https://doi.org/10.1023/a:1026328706869, 2004.

Haro-Monteagudo, D., Palazón, L., and Beguería, S.: Long-term sustainability of large water resource systems under climate change: A cascade modeling approach, Journal of Hydrology, 582, 124 546, https://doi.org/10.1016/j.jhydrol.2020.124546, 2020.

Hertrich, M., Braun, M., and Yaramanci, U.: Magnetic resonance soundings with separated transmitter and receiver loops, Near Surface Geophysics, 3, 141–154, https://doi.org/10.3997/1873-0604.2005010, 2005.

Immerzeel, W. W., Lutz, A. F., Andrade, M., Bahl, A., Biemans, H., Bolch, T., Hyde, S., Brumby, S., Davies, B. J., Elmore, A. C., Emmer, A., Feng, M., Fernández, A., Haritashya, U., Kargel, J. S., Koppes, M., Kraaijenbrink, P. D. A., Kulkarni, A. V., Mayewski, P. A., Nepal, S., Pacheco, P., Painter, T. H., Pellicciotti, F., Rajaram, H., Rupper, S., Sinisalo, A., Shrestha, A. B., Viviroli, D., Wada, Y., Xiao, C., Yao, T., and Baillie, J. E. M.: Importance and vulnerability of the world's water towers, Nature, 577, 364–369, https://doi.org/10.1038/s41586-019-1822-y, 2019.

Lajaunie, M., Gance, J., Sailhac, P., Malet, J., Warden, S., and Larnier, H.: Hydrogeological structure of a granitic mountain catchment inferred from multi-method electrical resistivity datasets, Near Surface Geophysics, 22, 26–46, https://doi.org/10.1002/nsg.12268, 2023.

Lataniotis, C., Marelli, S., and Sudret, B.: Uncertainty Quantification in the cloud with UQCloud, https://doi.org/10.3929/ETHZ-B-000495417, 2021.

Legchenko, A. and Shushakov, O.: Inversion of surface NMR data, GEOPHYSICS, 63, 75–84, https://doi.org/10.1190/1.1444329, 1998.

Legchenko, A. and Valla, P.: A review of the basic principles for proton magnetic resonance sounding measurements, Journal of Applied Geophysics, 50, 3–19, https://doi.org/10.1016/s0926-9851(02)00127-1, 2002.

Legchenko, A., Miège, C., Koenig, L. S., Forster, R. R., Miller, O., Solomon, D. K., Schmerr, N., Montgomery, L., Ligtenberg, S., and Brucker, L.: Investigating a firn aquifer near Helheim Glacier (South-Eastern Greenland) with magnetic resonance soundings and ground-penetrating radar, Near Surface Geophysics, 16, 411–422, https://doi.org/10.1002/nsg.12001, 2018.

Legchenko, A., Baltassat, J.-M., Duwig, C., Boucher, M., Girard, J.-F., Soruco, A., Beauce, A., Mathieu, F., Legout, C., Descloitres, M., and Gabriela Patricia, F. A.: Time-lapse magnetic resonance sounding measurements for numerical modeling of water flow in variably saturated media, Journal of Applied Geophysics, 175, 103 984, https://doi.org/10.1016/j.jappgeo.2020.103984, 2020.

https://doi.org/10.5194/egusphere-2026-3611
Preprint. Discussion started: 26 June 2026

Legchenko, A., Baltassat, J.-M., Abbas, M., Isch, A., Amraoui, N., Azaroual, M., Deparis, J., Ryckebusch, C., and Kessouri, P.: Monitoring unsaturated water flow using magnetic resonance soundings, Journal of Hydrology, 612, 128 318, https://doi.org/10.1016/j.jhydrol.2022.128318, 2022.

Lesparre, N., Girard, J.-F., Jeannot, B., Weill, S., Dumont, M., Boucher, M., Viville, D., Pierret, M.-C., Legchenko, A., and Delay, F.: Magnetic resonance sounding measurements as posterior information to condition hydrological model parameters: Application to a hard-rock headwater catchment, Journal of Hydrology, 587, 124 941, https://doi.org/10.1016/j.jhydrol.2020.124941, 2020.

Lesparre, N., Pasquet, S., and Ackerer, P.: Impacts of hydrofacies geometry designed from seismic refraction tomography on estimated hydrogeophysical variables, Hydrology and Earth System Sciences, 28, 873–897, https://doi.org/10.5194/hess-28-873-2024, 2024.

Li, K., Yan, J., Li, F., Lu, K., Yu, Y., Li, Y., Zhang, L., Wang, P., Li, Z., Yang, Y., and Wang, J.: Non-invasive geophysical methods for monitoring the shallow aquifer based on time-lapse electrical resistivity tomography, magnetic resonance sounding, and spontaneous potential methods, Scientific Reports, 14, https://doi.org/10.1038/s41598-024-58062-2, 2024.

Lindström, G., Johansson, B., Persson, M., Gardelin, M., and Bergström, S.: Development and test of the distributed HBV-96 hydrological model, Journal of Hydrology, 201, 272–288, https://doi.org/10.1016/s0022-1694(97)00041-3, 1997.

Lubczynski, M. and Roy, J.: Hydrogeological interpretation and potential of the new magnetic resonance sounding (MRS) method, Journal of Hydrology, 283, 19–40, https://doi.org/10.1016/s0022-1694(03)00170-7, 2003.

Maina, F. Z. and Guadagnini, A.: Uncertainty Quantification and Global Sensitivity Analysis of Subsurface Flow Parameters to Gravimetric Variations During Pumping Tests in Unconfined Aquifers, Water Resources Research, 54, 501–518, https://doi.org/10.1002/2017wr021655, 2018.

Mazzilli, N., Chalikakis, K., Carrière, S. D., and Legchenko, A.: Surface Nuclear Magnetic Resonance Monitoring Reveals Karst Unsaturated Zone Recharge Dynamics during a Rain Event, Water, 12, 3183, https://doi.org/10.3390/w12113183, 2020.

Moraga, J. S., Peleg, N., Fatichi, S., Molnar, P., and Burlando, P.: Revealing the impacts of climate change on mountainous catchments through high-resolution modelling, Journal of Hydrology, 603, 126 806, https://doi.org/10.1016/j.jhydrol.2021.126806, 2021.

Moua, R., Lesparre, N., Girard, J.-F., Belfort, B., Lehmann, F., and Younes, A.: Coupled hydrogeophysical inversion of an artificial infiltration experiment monitored with ground-penetrating radar: synthetic demonstration, Hydrology and Earth System Sciences, 27, 4317–4334, https://doi.org/10.5194/hess-27-4317-2023, 2023.

Mualem, Y.: A new model for predicting the hydraulic conductivity of unsaturated porous media, Water resources research, 12, 513–522, https://doi.org/10.1029/wr012i003p00513, 1976.

Oursin, M., Pierret, M.-C., Beaulieu, E., Daval, D., and Legout, A.: Is there still something to eat for trees in the soils of the Strengbach catchment?, Forest Ecology and Management, 527, 120 583, https://doi.org/10.1016/j.foreco.2022.120583, 2023.

Pasquet, S., Marçais, J., Hayes, J. L., Sak, P. B., Ma, L., and Gaillardet, J.: Catchment-Scale Architecture of the Deep Critical Zone Revealed by Seismic Imaging, Geophysical Research Letters, 49, https://doi.org/10.1029/2022gl098433, 2022.

Pierret, M.-C., Cotel, S., Ackerer, P., Beaulieu, E., Benarioumlil, S., Boucher, M., Boutin, R., Chabaux, F., Delay, F., Fourtet, C., Friedmann, P., Fritz, B., Gangloff, S., Girard, J.-F., Legtchenko, A., Viville, D., Weill, S., and Probst, A.: The Strengbach Catchment: A Multidisciplinary Environmental Sentry for 30 Years, Vadose Zone Journal, 17, 1–17, https://doi.org/10.2136/vzj2018.04.0090, 2018.

Pleasants, M. S., Neves, F. d. A., Parsekian, A. D., Befus, K. M., and Kelleners, T. J.: Hydrogeophysical Inversion of Time-Lapse ERT Data to Determine Hillslope Subsurface Hydraulic Properties, Water Resources Research, 58, https://doi.org/10.1029/2021wr031073, 2022.

Razavi, S., Jakeman, A., Saltelli, A., Prieur, C., Iooss, B., Borgonovo, E., Plischke, E., Lo Piano, S., Iwanaga, T., Becker, W., Tarantola, S., Guillaume, J. H., Jakeman, J., Gupta, H., Melillo, N., Rabitti, G., Chabridon, V., Duan, Q., Sun, X., Smith, S., Sheikholeslami, R.,

https://doi.org/10.5194/egusphere-2026-3611
Preprint. Discussion started: 26 June 2026

Hosseini, N., Asadzadeh, M., Puy, A., Kucherenko, S., and Maier, H. R.: The Future of Sensitivity Analysis: An essential discipline for systems modeling and policy support, Environmental Modelling amp; Software, 137, 104 954, https://doi.org/10.1016/j.envsoft.2020.104954, 2021.

Richards, L. A.: Capillary conduction of liquids through porous mediums, physics, 1, 318–333, https://doi.org/10.1063/1.1745010, 1931.

Rouzies, E., Lauvernet, C., Sudret, B., and Vidard, A.: How is a global sensitivity analysis of a catchment-scale, distributed pesticide transfer model performed? Application to the PESHMELBA model, Geoscientific Model Development, 16, 3137–3163, https://doi.org/10.5194/gmd-16-3137-2023, 2023.

Saltelli, A., Tarantola, S., Campolongo, F., and Ratto, M.: Sensitivity Analysis in Practice: A Guide to Assessing Scientific Models, Wiley, ISBN 9780470870952, https://doi.org/10.1002/0470870958, 2002.

Saltelli, A., Ratto, M., Andres, T., Campolongo, F., Cariboni, J., Gatelli, D., Saisana, M., and Tarantola, S.: Global Sensitivity Analysis. The Primer, Wiley, ISBN 9780470725184, https://doi.org/10.1002/9780470725184, 2007.

Sobol, I.: Global sensitivity indices for nonlinear mathematical models and their Monte Carlo estimates, Mathematics and Computers in Simulation, 55, 271–280, https://doi.org/10.1016/s0378-4754(00)00270-6, 2001.

Soize, C. and Ghanem, R.: Physical Systems with Random Uncertainties: Chaos Representations with Arbitrary Probability Measure, SIAM Journal on Scientific Computing, 26, 395–410, https://doi.org/10.1137/s1064827503424505, 2004.

Song, X., Zhang, J., Zhan, C., Xuan, Y., Ye, M., and Xu, C.: Global sensitivity analysis in hydrological modeling: Review of concepts, methods, theoretical framework, and applications, Journal of Hydrology, 523, 739–757, https://doi.org/10.1016/j.jhydrol.2015.02.013, 2015.

Strohmenger, L., Ackerer, P., Belfort, B., and Pierret, M.: Local and seasonal climate change and its influence on the hydrological cycle in a mountainous forested catchment, Journal of Hydrology, 610, 127 914, https://doi.org/10.1016/j.jhydrol.2022.127914, 2022.

Sudret, B.: Global sensitivity analysis using polynomial chaos expansions, Reliability Engineering amp; System Safety, 93, 964–979, https://doi.org/10.1016/j.ress.2007.04.002, 2008.

Tang, F. H. M., Lenzen, M., McBratney, A., and Maggi, F.: Risk of pesticide pollution at the global scale, Nature Geoscience, 14, 206–210, https://doi.org/10.1038/s41561-021-00712-5, 2021.

Van Genuchten, M. T.: A closed-form equation for predicting the hydraulic conductivity of unsaturated soils, Soil science society of America journal, 44, 892–898, https://doi.org/10.2136/sssaj1980.03615995004400050002x, 1980.

Virtanen, P., Gommers, R., Oliphant, T. E., Haberland, M., Reddy, T., Cournapeau, D., Burovski, E., Peterson, P., Weckesser, W., Bright, J., van der Walt, S. J., Brett, M., Wilson, J., Millman, K. J., Mayorov, N., Nelson, A. R. J., Jones, E., Kern, R., Larson, E., Carey, C. J., Polat, , Feng, Y., Moore, E. W., VanderPlas, J., Laxalde, D., Perktold, J., Cimrman, R., Henriksen, I., Quintero, E. A., Harris, C. R., Archibald, A. M., Ribeiro, A. H., Pedregosa, F., van Mulbregt, P., Vijaykumar, A., Bardelli, A. P., Rothberg, A., Hilboll, A., Kloeckner, A., Scopatz, A., Lee, A., Rokem, A., Woods, C. N., Fulton, C., Masson, C., Häggström, C., Fitzgerald, C., Nicholson, D. A., Hagen, D. R., Pasechnik, D. V., Olivetti, E., Martin, E., Wieser, E., Silva, F., Lenders, F., Wilhelm, F., Young, G., Price, G. A., Ingold, G.-L., Allen, G. E., Lee, G. R., Audren, H., Probst, I., Dietrich, J. P., Silterra, J., Webber, J. T., Slavič, J., Nothman, J., Buchner, J., Kulick, J., Schönberger, J. L., de Miranda Cardoso, J. V., Reimer, J., Harrington, J., Rodríguez, J. L. C., Nunez-Iglesias, J., Kuczynski, J., Tritz, K., Thoma, M., Newville, M., Kümmerer, M., Bolingbroke, M., Tartre, M., Pak, M., Smith, N. J., Nowaczyk, N., Shebanov, N., Pavlyk, O., Brodtkorb, P. A., Lee, P., McGibbon, R. T., Feldbauer, R., Lewis, S., Tygier, S., Sievert, S., Vigna, S., Peterson, S., More, S., Pudlik, T., Oshima, T., Pingel, T. J., Robitaille, T. P., Spura, T., Jones, T. R., Cera, T., Leslie, T., Zito, T., Krauss, T., Upadhyay, U., Halchenko,

https://doi.org/10.5194/egusphere-2026-3611
Preprint. Discussion started: 26 June 2026

Y. O., and Vázquez-Baeza, Y.: SciPy 1.0: fundamental algorithms for scientific computing in Python, Nature Methods, 17, 261–272, https://doi.org/10.1038/s41592-019-0686-2, 2020.

Viviroli, D., Archer, D. R., Buytaert, W., Fowler, H. J., Greenwood, G. B., Hamlet, A. F., Huang, Y., Koboltschnig, G., Litaor, M. I., López-Moreno, J. I., Lorentz, S., Schädler, B., Schreier, H., Schwaiger, K., Vuille, M., and Woods, R.: Climate change and mountain water resources: overview and recommendations for research, management and policy, Hydrology and Earth System Sciences, 15, 471–504, https://doi.org/10.5194/hess-15-471-2011, 2011.

Viviroli, D., Kummu, M., Meybeck, M., Kallio, M., and Wada, Y.: Increasing dependence of lowland populations on mountain water resources, Nature Sustainability, 3, 917–928, https://doi.org/10.1038/s41893-020-0559-9, 2020.

Wiener, N.: The Homogeneous Chaos, American Journal of Mathematics, 60, 897, https://doi.org/10.2307/2371268, 1938.

Wu, X., Shirvan, K., and Kozlowski, T.: Demonstration of the relationship between sensitivity and identifiability for inverse uncertainty quantification, Journal of Computational Physics, 396, 12–30, https://doi.org/10.1016/j.jcp.2019.06.032, 2019.

Yates, L. A., Aandahl, Z., Richards, S. A., and Brook, B. W.: Cross validation for model selection: A review with examples from ecology, Ecological Monographs, 93, https://doi.org/10.1002/ecm.1557, 2023.

Younes, A., Zaouali, J., Lehmann, F., and Fahs, M.: Sensitivity and identifiability of hydraulic and geophysical parameters from streaming potential signals in unsaturated porous media, Hydrology and Earth System Sciences, 22, 3561–3574, https://doi.org/10.5194/hess-22-3561-2018, 2018.

Zhang, M., Feng, X., Bano, M., Xing, H., Wang, T., Liang, W., Zhou, H., Dong, Z., An, Y., and Zhang, Y.: Review of Ground Penetrating Radar Applications for Water Dynamics Studies in Unsaturated Zone, Remote Sensing, 14, 5993, https://doi.org/10.3390/rs14235993, 2022.

Šimůnek, J., van Genuchten, M. T., and Šejna, M.: Development and Applications of the HYDRUS and STANMOD Software Packages and Related Codes, Vadose Zone Journal, 7, 587–600, https://doi.org/10.2136/vzj2007.0077, 2008.